PRFXeption: Multisource LiDAR-Supervised Sentinel-2 Learning for 10-m Canopy-Height Mapping in Giant-Tree Regions

Guangpeng Fan, Binghong Zhang, Fei Yan, Haoran Zhao, Liangliang Xu, Jiani Guo, Jialing Zhou, Xiangyu Ma, Jinhu Wang, Zhiwei Zhang, Yan Zhang, MeiRong Bao, Riqian Zhao, Jia Wang, and Liangliang Nan

***Abstract*—Giant trees represent the upper limits of terrestrial plant growth; yet, their regional distribution remains poorly constrained because existing canopy-height products often compress the upper tail, whereas spaceborne light detection and ranging (LiDAR) provides spatially discontinuous observations. We developed PRFXeption, a sparse-supervised patch-to-pixel framework in which Sentinel-2 imagery provides spatially continuous inputs and canopy-height References from nearly 20 million global ecosystem dynamics investigation (GEDI) footprints, and approximately 5.8 million unmanned aerial vehicle (UAV) and airborne LiDAR samples across 27 sites provide structural supervision. The model was applied to 24 landscapes in northwestern North America, southeastern Australia, Southeast Asia, and southeastern Tibet–northwestern Yunnan to generate continuous 10-m canopy-height maps. Independent evaluations yielded RMSEs of 5.19 m against UAV/airborne LiDAR, 6.94 m against forest inventory measurements, and 7.86–9.35 m across four spatially independent GEDI regional test subsets. Prediction errors increased on slopes exceeding approximately 30°, and the tallest canopies remained moderately underestimated. Receptive-field experiments revealed a task-dependent tradeoff: the 3×3 configuration minimized full-distribution error, whereas the validation-selected multiscale configuration showed lower pooled upper tail errors in independent testing. The resulting maps preserved spatially coherent high-canopy patterns and, together with high-resolution optical imagery, highlighted two candidate communities not represented in the field records available to this study. Subsequent UAV LiDAR confirmed trees taller than 60 m at both sites, including trees exceeding 70 m at one site. The mapped patterns further support southeastern Tibet–northwestern Yunnan as a candidate fourth major global concentration of giant trees. These results demonstrate the potential of multisource LiDAR-supervised optical learning for continuous canopy-height mapping and satellite-guided screening of rare tall-canopy landscapes.**

***Index Terms*—Canopy-height mapping, deep learning, giant-tree communities, light detection and ranging (LiDAR), multisource remote sensing, Sentinel-2, sparse supervision.**

Received 23 July 2026; revised 23 September 2026; accepted 12 October 2026. Date of publication 19 October 2026; date of current version 5 November 2026. This work was supported in part by Beijing High Innovation Plan through the Young Elite Scientists Sponsorship Program under Grant 20250859, in part by Guangxi Forestry Science and Technology Extension Project under Grant 2024GXLK08, in part by The Science and Technology Plan of Hinggan League Science and Technology Bureau under Grant MBHZ2025010 and Grant MBJH2024019, and in part by the Key Project of National Natural Science Foundation of China under Grant 42330507. *(Corresponding author: Jia Wang.)*

Guangpeng Fan is with the School of Information Science and Technology, Beijing Forestry University, Beijing 100083, China, also with Hebei Key Laboratory of Smart National Park, Beijing 070001, China, and also with Beijing Key Laboratory of Precision Forestry, Beijing Forestry University, Beijing, China (e-mail: fgp1994@bjfu.edu.cn).

Binghong Zhang, Haoran Zhao, Liangliang Xu, Jiani Guo, and Xiangyu Ma are with the School of Information Science and Technology, Beijing Forestry University, Beijing 100083, China (e-mail: fenglaosir@bjfu.edu.cn; haoran01@bjfu.edu.cn; xuliangliang@bjfu.edu.cn; jianiguo905@bjfu.edu.cn; maxiangyu@bjfu.edu.cn).

Fei Yan and Jia Wang are with Beijing Key Laboratory of Precision Forestry, Beijing Forestry University, Beijing 100083, China (e-mail: yanfei522@bjfu.edu.cn; wangjia2009@bjfu.edu.cn).

Jialing Zhou is with the School of Information Science and Technology, Beijing Forestry University, Beijing, China, and also with the School of Computer Science and Engineering, Northeastern University, Shenyang 110819, China (e-mail: zhoujialing@bjfu.edu.cn).

Jinhu Wang is with the Institute for Biodiversity and Ecosystem Dynamics (IBED), University of Amsterdam, 1012 WP Amsterdam, The Netherlands (e-mail: j.wang7@uva.nl).

Zhiwei Zhang is with the Key Laboratory of Forest Ecology in Tibet Plateau, College of Resources and Environmental Sciences, Tibet Agricultural and Animal Husbandry University, Nyingchi, Tibet 860000, China (e-mail: aiwoweige@163.com).

Yan Zhang is with Xing'an League Institute of Forestry, Ulanhot, Inner Mongolia 137400, China (e-mail: 905209104@qq.com).

MeiRong Bao and Riqian Zhao are with Xing'an Polytechnic University, Ulanhot, Inner Mongolia 137700, China (e-mail: xazyjsxykjc@126.com; zrq514266@sina.com).

Liangliang Nan is with the Urban Data Science Section, Delft University of Technology, 2628 CD Delft, The Netherlands (e-mail: liangliang.nan@tudelft.nl).

This article has supplementary downloadable material available at https://doi.org/10.1109/TGRS.2026.3744696, provided by the authors.

Digital Object Identifier 10.1109/TGRS.2026.3744696

I. Introduction

Giant trees are rare but disproportionately important components of forest ecosystems. Their exceptional vertical structure creates heterogeneous habitats for birds, insects, fungi, epiphytes, and other organisms, while their large biomass contributes to long-term carbon storage, forest structural complexity [1], [2], and ecosystem stability. Forests containing giant trees therefore represent high-value targets for biodiversity conservation, carbon-cycle research, and long-term ecosystem monitoring [3], [4].

Exceptionally tall trees have historically been documented primarily in three regions: the coastal forests of northwestern North America from California to British Columbia, the tall eucalyptus forests of southeastern Australia, and the tropical rainforests of Southeast Asia. In 2023, the discovery of a 102.3-m Tibetan cypress in southeastern Tibet provided direct evidence that the eastern Himalayan region supports some of the tallest documented trees in Asia [5]. Together with other recently documented tall trees in southeastern Tibet and northwestern Yunnan, this finding suggests that the region may represent a candidate fourth major global concentration of giant trees. However, the spatial extent, continuity, and internal distribution of these exceptionally tall forests remain incompletely characterized.

© 2026 The Authors. This work is licensed under a Creative Commons Attribution 4.0 License.
For more information, see https://creativecommons.org/licenses/by/4.0/

Systematic investigation of giant-tree landscapes is difficult because many candidate forests occur in remote, mountainous, and poorly accessible regions. Ground surveys and unmanned aerial vehicle (UAV) light detection and ranging (LiDAR) provide accurate measurements of individual trees and local forest structure, but their spatial coverage is limited, and their implementation is costly at regional scales. Continuous canopy-height mapping can complement these observations by identifying localized tall-forest patterns and prioritizing candidate areas for targeted UAV and field investigation. Existing national and global canopy-height products provide valuable information on broad forest structure, but they frequently underestimate or compress the upper tail of the canopy-height distribution in tall, dense, and topographically complex forests [3], [6], [7]. Such limitations can arise from optical saturation, coarse spatial support, geolocation uncertainty, insufficient representation of extreme-height references, and mismatch between LiDAR footprints and optical pixels. Consequently, products optimized for broad geographical consistency may not retain sufficient sensitivity for screening rare, spatially localized tall-canopy features.

Satellite remote sensing provides an efficient means of characterizing forest structure from regional to continental scales and can complement field measurements and high-resolution UAV or airborne LiDAR observations [8]. Since 2019, the global ecosystem dynamics investigation (GEDI) has provided direct full-waveform observations of forest vertical structure [9], [10], but its footprint sampling is spatially discontinuous and cannot independently provide wall-to-wall canopy-height coverage. Sentinel-2 provides spatially continuous multispectral imagery at native spatial resolutions of 10–60 m and offers complementary information on canopy reflectance, texture, and landscape context. Data-driven remote sensing approaches have demonstrated the potential of optical imagery for tree-crown and height characterization [11], while harmonized structural products have highlighted the value and scale dependence of large-area remote sensing observations [12]. Previous studies have further demonstrated the utility of integrating sparse LiDAR measurements with spatially continuous optical or radar observations for large-area canopy-height mapping [13], [14].

Recent studies have extended these approaches using high-resolution and multisource observations. Multiple machine learning regression models have been applied to UAV-LiDAR-derived structural features for tree-height retrieval [15]. UAV hyperspectral point clouds have enabled direct 3-D integration of spectral and structural information for vegetation characterization [16], while multisource frameworks combining UAV LiDAR, Sentinel-1 SAR, and stereo optical imagery have demonstrated complementary sensitivity to vegetation height and aboveground structure [17]. These studies demonstrate the potential of data-driven spectral–structural integration at local to regional scales. However, extending geographically sparse structural references to spatially continuous 10-m satellite mapping across widely separated giant-tree landscapes remains challenging.

The present study addresses this different but related setting: spatially continuous satellite inference under geographically sparse structural supervision. Sentinel-2 constitutes the wall-to-wall model input, whereas GEDI, UAV LiDAR, and airborne LiDAR provide canopy-height references only at a subset of locations. We therefore use the term multisource LiDAR supervision to distinguish this supervision-level integration from direct data- or feature-level fusion. Four methodological challenges are particularly relevant in giant-tree regions [18]. First, valid canopy-height labels are available only at GEDI footprints and within areas covered by UAV or airborne LiDAR, resulting in a sparse-label regression problem [19]. Second, reference observations are strongly imbalanced across the canopy-height distribution, with relatively few samples representing the extreme upper tail; regression toward the mean can therefore suppress the tallest canopies [20]. Third, giant-tree regions differ markedly in forest composition, crown architecture, climate, terrain, and sensor-acquisition conditions, complicating the application of a common model across geographically separated landscapes [21]. Fourth, an individual 10-m optical pixel contains limited structural information, whereas rare tall-canopy patches may be better represented by combining local spectral and crown-scale cues with broader stand-level spatial context [22].

For giant-tree screening, the model with the lowest average prediction error is not necessarily the model with the greatest utility for tall-canopy screening [23]. Full-distribution RMSE is dominated by the more abundant low- and intermediate-height observations and may therefore obscure weak sensitivity to rare extreme-height canopies. A model can achieve relatively low average error while continuing to underestimate the upper tail through regression toward the mean. Canopy-height mapping for giant-tree screening must therefore balance general regression accuracy with sensitivity to rare, spatially localized high-canopy features.

To address these challenges, we developed PRFXeption, a sparse-supervised patch-to-pixel learning framework that transfers geographically distributed LiDAR-derived canopy-height references to spatially continuous Sentinel-2 mapping at 10-m resolution. The methodological contribution of PRFXeption lies primarily in this learning framework rather than in any individual convolutional operator. Sentinel-2 imagery constitutes the spatially continuous model input, whereas canopy heights derived from GEDI, UAV LiDAR, and airborne LiDAR provide spatially sparse structural supervision during model development and evaluation. LiDAR observations are therefore not required as inference-time inputs. By exploiting the spatial neighborhood surrounding each target pixel, the framework integrates pixel-level spectral information with crown- and stand-level spatial context. Detailed architectural implementation, including the patch size, receptive-field branches, residual learning, and depthwise-separable convolution, is presented in Section III.

Accordingly, we treated full-distribution accuracy and extreme-height sensitivity as complementary evaluation objectives rather than assuming that a single-receptive-field configuration would be optimal for all applications. Receptive-field configurations were compared under a task-oriented evaluation framework, with particular attention to their ability to retain the sparsely represented upper canopy-height tail relevant to giant-tree screening.

The model was trained and evaluated using nearly 20 million GEDI footprint observations and approximately 5.8 million samples derived from UAV and airborne LiDAR across 27 sites. PRFXeption was subsequently applied to 24 landscapes distributed across northwestern North America, southeastern Australia, Southeast Asia, and southeastern Tibet–northwestern Yunnan to generate continuous canopy-height maps at 10-m resolution.[1] Model reliability was evaluated using complementary GEDI, UAV, and airborne LiDAR, and forest inventory references [24]. GEDI-based evaluations were conducted in four representative regional test areas, while UAV or airborne LiDAR and forest inventory measurements provided independent higher-resolution and ground-based assessments. We further examined height-dependent prediction behavior, terrain-related uncertainty, and differences among receptive-field configurations. The resulting maps were interpreted as regional screening products for identifying candidate tall-canopy landscapes rather than as direct measurements of individual giant trees.

The objectives of this study were to: 1) develop a sparse multisource LiDAR-supervised learning framework for 10-m Sentinel-2 canopy-height estimation in major giant-tree regions; 2) evaluate prediction reliability using GEDI, UAV and airborne LiDAR, and forest inventory observations; 3) quantify the effects of canopy-height range, terrain slope, and receptive-field configuration on prediction behavior; 4) distinguish full-distribution regression performance from sensitivity to the extreme upper tail of the canopy-height distribution; 5) generate continuous canopy-height maps for geographically separated giant-tree landscapes; and 6) assess whether the mapped tall-canopy patterns can guide the identification and subsequent confirmation of candidate giant-tree communities.

The principal contributions of this study are summarized as follows.

1) We formulate 10-m canopy-height mapping as sparse multisource LiDAR-supervised patch-to-pixel regression, enabling geographically discontinuous structural references to support spatially continuous Sentinel-2 prediction without requiring LiDAR observations as inference-time inputs.
2) We introduce a task-oriented evaluation strategy that explicitly distinguishes full-distribution canopy-height accuracy from sensitivity to the extreme upper tail, thereby revealing the tradeoff between locally optimized and multiscale spatial-context configurations.
3) We constructed a geographically diverse canopy-height reference dataset comprising nearly 20 million GEDI footprints and approximately 5.8 million UAV and airborne LiDAR samples across 27 sites, and evaluated the resulting 10-m canopy-height estimates using complementary GEDI, UAV/airborne LiDAR, and forest inventory observations across contrasting giant-tree regions.
4) We demonstrate the use of continuous canopy-height maps as a regional screening tool by identifying two candidate giant-tree communities not represented in the field records and literature considered in this study, both of which were subsequently confirmed using UAV LiDAR. The mapped patterns further provide spatial evidence supporting consideration of southeastern Tibet–northwestern Yunnan as a candidate fourth major global concentration of giant trees.

[1]The canopy-height maps are available at: https://ee-fenglaosir.projects.earthengine.app/view/global-giant-tree-areas-canopy-height

II. Study Areas and Datasets

A. Study Areas

The study covered four broad regions containing documented or emerging evidence of exceptionally tall forests: northwestern North America, Southeast Asia [25], southeastern Australia, and southeastern Tibet–northwestern Yunnan in China [26] (see Fig. 1). These regions encompass temperate rainforests, tropical dipterocarp forests, montane coniferous forests, and tall eucalyptus forests, thereby representing substantial variation in forest composition, canopy architecture, climate, and terrain. The regional areas reported below refer to the geographic extents of the analysis domains shown in Fig. 1 rather than formal biological boundaries of global giant-tree distribution centers. These domains encompass the principal documented or emerging tall-tree landscapes considered in this study and provide contrasting environmental settings for evaluating canopy-height mapping.

1) *Southeast Tibet and Northwest Yunnan*. This recently identified region spans over 332 000 km^2 and contains a unique mix of tropical and temperate rainforests. The Yarlung Zangbo Grand Canyon, the world's deepest, contributes to extreme vertical climate gradients and extraordinary biodiversity [27]. Recent field surveys have revealed record-breaking trees, including a 102.3-m Tibetan cypress, the tallest tree in Asia, as well as a 76.8-m Bhutan pine and an 83.4-m yellow fir [5]. These findings highlight the global significance of this area as a giant-tree distribution center.
2) *Northwest America:* Extending from California to British Columbia, this 233 000 km^2 region contains some of the tallest trees on Earth, including the iconic coast redwoods that define much of the region's forest structure.
3) *Southeast Asia*. Concentrated in Borneo and covering approximately 177 000 km^2, these forests host diverse tropical tree species, many of which form towering canopies that remain poorly documented due to limited accessibility.
4) *Southeast Australia:* This 179 000-km^2 region, particularly Tasmania, is dominated by eucalyptus species that are among the tallest flowering plants in the world, forming distinctive giant-tree communities.

The four domains represent contrasting environmental and structural settings associated with exceptionally tall forests: coastal temperate redwood forests in northwestern North America, humid tropical dipterocarp forests in Southeast Asia, tall eucalyptus forests in southeastern Australia, and

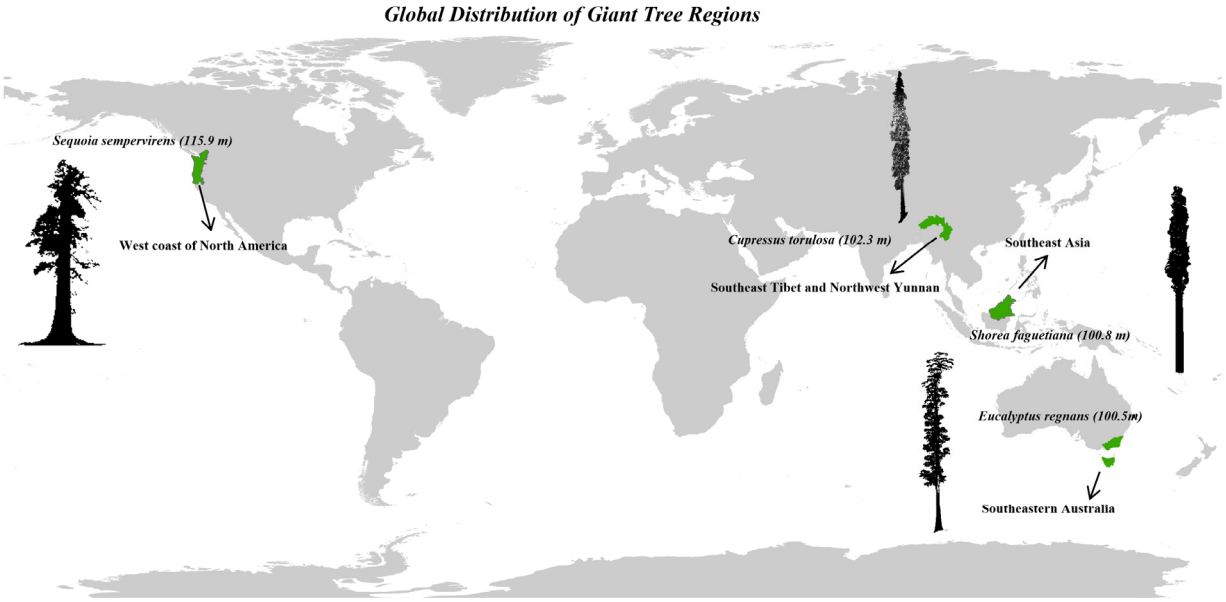


Fig. 1. Four global giant tree areas considered in this study: northwestern North America, southeastern Australia, Southeast Asia, and southeastern Tibet–northwestern Yunnan.

strongly mountainous tropical-to-temperate forests in southeastern Tibet–northwestern Yunnan. The latter spans extreme elevational gradients under strong monsoon influence and contains recently documented trees reaching 76.8–102.3 m. These contrasts in climate, topography, forest type, and canopy structure provide geographically diverse conditions for model evaluation. The analysis targets representative tall-forest landscapes rather than formally delineating all global giant-tree forests. 7

B. Datasets

Discovering giant-tree communities requires multisource observations that capture forest vertical structure across multiple spatial scales, from individual trees and local plots to regional and global landscapes. Therefore, we integrated ground-based forest inventories, UAV and airborne LiDAR, spaceborne LiDAR from GEDI, and Sentinel-2 multispectral imagery. These datasets provide the complementary structural and spectral information, enabling accurate canopy-height estimation, large-scale mapping, and ecological interpretation of giant-tree ecosystems.

1) *Field Data:* Ground surveys were conducted in southeastern Tibet in 2020 following the National Forest Resource Inventory Standards. A total of 227 fixed and temporary plots were established using a 6×8 km sampling grid, with each plot covering 0.0667 hm^2. Due to accessibility constraints, plots located in highly inaccessible areas were randomly relocated. The surveyed plots covered a wide range of forest conditions, with tree densities ranging from 165 to 2474 trees ha^{-1}.
   Plot centers were georeferenced using RTK GNSS with centimeter-level accuracy. Tree locations were measured using azimuth–distance methods based on laser rangefinders and electronic compasses. For areas with weak satellite signals, GNSS receivers were relocated to open canopy locations, and repeated measurements were collected to improve positioning reliability. Species identity, tree height, and structural attributes were recorded for each plot, and average heights of dominant species were calculated for validation. The plot boundary measurement error was less than 0.5%, relative tree position errors were within 3%, and tree height measurement errors were less than 3% for trees below 10 m and less than 5% for taller trees. These field observations provided independent references for evaluating canopy-height predictions and confirming candidate giant-tree communities. Because the 0.0667-ha inventory plots and 10-m prediction pixels differ in spatial support, field-derived dominant-tree height was treated as an independent cross-scale reference rather than as pixel-identical ground truth. Field inventories were available only in southeastern Tibet, where the authors conducted a dedicated ground survey of giant-tree landscapes. Comparable plot-level inventories were not available for the other three regional domains; therefore, these field data were used only as an independent regional validation reference. Representative field-survey photographs are provided in Fig. S1.
2) *UAV-LS and ALS Point Clouds:* High-resolution LiDAR datasets were used to characterize forest 3-D structures and provide accurate canopy-height references for model training, validation, and cross-scale evaluation. We integrated three public airborne LiDAR (ALS) datasets and one UAV-based LiDAR scanning (UAV-LS) dataset covering representative giant-tree regions worldwide (Table I). The ALS datasets included observations from North America (G-LiHT and USGS), Australia

TABLE I

OVERVIEW OF SENSOR PARAMETERS USED FOR THE DATASETS IN THIS STUDY. NORTH AMERICAN DATA OBTAINED BY RIEGL LD321-A40 AND LEICA ALS50 PHASE-II LIDAR SYSTEMS; AUSTRALIAN DATA FROM TRIMBLE AX60, LEICA ALS80, OPTECH PEGASUS, AND GEMINI; WHILE SOUTHEAST ASIAN DATA FROM OPTECH ORION M300

Laser scanner	Optech Orion m300	Riegl LD321-A40	Leica ALS50 Phase II	Trimble AX60	Leica ALS80	Optech Pegasus/Gemini
Flight altitude (m)	100∼2500	∼335	900	850	∼3000	150∼5000
Beam divergence (mrad)	0.25	0.3	0.5	0.25	0.2	0.25
Maximum scan angle (°)	0∼50	±30	±15	40	±30	75/50
Footprint size (cm)	12	50	28	15	11	17
Point density (points/m^2)	4∼10	∼30	≥8	4	0.5	3
Along-track resolution (m)	<0.7	0.5	∼0.9	0.4	0.6	0.7

(Forest2019, Jacobs River, North West, and Central Highlands [28]), and Southeast Asia (Carbon Monitoring System).[2] These airborne LiDAR datasets provided regional-scale measurements of forest vertical structure and complemented the sparse but globally distributed GEDI observations.

To capture detailed canopy structures in southeastern Tibet, we collected an unpublished UAV-LS dataset using a DJI Zenmuse L1 LiDAR sensor mounted on a DJI Matrice 300 RTK platform. The Zenmuse L1 integrates LiDAR scanning, RGB imaging, and a stabilized gimbal, providing a 20-Mpixel camera, three-return scanning capability, and a maximum scanning rate of 480 000 points s^{-1}. The multireturn LiDAR system enables laser penetration through dense forest canopies and accurate measurement of ground and vegetation structures, which is essential for reconstructing the complex vertical profiles of giant-tree forests. UAV-LS surveys covered more than 1 500 000 m^2 across representative sites in southeastern Tibet.

All UAV-LS and ALS point clouds were processed using LiDAR360 V5.4 [29]. The preprocessing workflow included noise removal, ground-point classification, removal of nonvegetation objects, and height normalization. Canopy-height models (CHMs) were subsequently generated from the normalized vegetation point clouds using digital elevation and surface models. To ensure consistency between airborne and spaceborne LiDAR observations, normalized UAV-LS point clouds were further processed using rGEDI [30] to simulate GEDI-like waveforms and derive relative height metrics.

Overall, LiDAR observations from 27 representative sites were consistently processed, including 12 sites in southeastern Tibet and five sites each in North America, Australia, and Southeast Asia. The resulting CHMs and LiDAR-derived structural metrics provided high-resolution references for canopy-height estimation and enabled the integration of fine-scale 3-D observations with satellite-based continuous mapping. Detailed information on LiDAR sensors and acquisition parameters is provided in Table I. Although different LiDAR systems were used, all point clouds underwent the same preprocessing and height-normalization workflow, and supervision was derived from ground-relative canopy-height measurements rather than raw range or intensity data. Direct intersensor bias correction was not applied because common contemporaneous calibration sites were unavailable.

3) *GEDI L1B and 2A Data:* GEDI provides full-waveform observations with an approximately 25-m footprint diameter rather than a 25-m raster resolution, measuring 10 billion waveforms, each up to 1420 vertical elements in length with a 1 ns (∼15 cm) interval [31]. We utilized GEDI Version 2 and analyzed 1613 L1B products collected between April 2019 and August 2020 across the study regions. Systematic geolocation errors were corrected by aligning observed GEDI waveforms with simulated waveforms. Using rGEDI [30], normalized UAV-LS and ALS point clouds were converted into simulated waveforms through Gaussian convolution, from which corresponding canopy heights were derived. A deep convolutional neural network was then trained to map L1B waveform features to canopy height using reference targets from GEDI L2A RH98 measurements and UAV-LS/ALS-derived simulated waveform–height pairs, depending on the specific training task. GEDI L2A RH98 was used as the footprint-scale relative-height reference corresponding to quality-controlled L1B observations, while the UAV-LS/ALS data provided independent high-resolution structural references for waveform-based model development. GEDI L2A and L2B additionally provide footprint-scale canopy-height and vertical-profile information, including longitude, latitude, ground elevation, and relative-height metrics [32]. Invalid L1B waveforms were excluded using the *quality_flag* attribute before constructing the waveform-to-height training datasets.

4) *Sentinel-2 Imagery:* Sentinel-2A and Sentinel-2B carry the Multispectral Instrument, which acquires 13 spec-

[2]ALS data available at: Australia: https://elevation.fsdf.org.au/; America: https://apps.nationalmap.gov/downloader/; Southeast Asia: https://daac.ornl.gov/orders/

tral bands at native spatial resolutions of 10, 20, and 60 m with an approximately five-day revisit interval [33], [34]. We acquired 206 scenes with reported cloud cover below 20% from the Copernicus Data Space for southeastern Tibet–northwestern Yunnan, northwestern North America, Southeast Asia, and southeastern Australia between April 2019 and August 2021.[3] The imagery was processed to Level-2A surface reflectance using Sen2Cor within the Sentinel Application Platform [35].

Twelve spectral bands were used as model inputs: B02, B03, B04, and B08 at 10 m; B05–B07, B8A, B11, and B12 at 20 m; and B01 and B09 at 60 m. No explicit feature-selection algorithm was applied. B10 was excluded because it is primarily intended for cirrus detection, whereas B01 was retained as part of the multispectral input without assuming an independent contribution to canopy-height retrieval. The 20- and 60-m bands were bilinearly resampled to the common 10-m grid.

Cloud-contaminated and invalid pixels were removed using the Sen2Cor Scene Classification Layer. Pixels classified as no-data, saturated or defective, cloud shadow, medium- or high-probability cloud, thin cirrus, or snow and ice were excluded. The quality-controlled scenes were subsequently mosaicked by landscape in QGIS and partitioned into image tiles for model training and wall-to-wall prediction, resulting in 2,412 JP2 files covering the selected giant-tree landscapes.

Together, these datasets supported continuous canopy-height mapping across the selected giant-tree landscapes and provided the multiscale observations required for regional screening and targeted UAV confirmation.

III. Methodology

A. Sparse LiDAR Supervision and Spatial Association With Sentinel-2

In this study, multisource LiDAR and Sentinel-2 observations were integrated at the supervision level rather than through direct data- or feature-level fusion. Sentinel-2 imagery constitutes the spatially continuous model input, whereas canopy-height measurements derived from GEDI, UAV LiDAR, and airborne LiDAR provide spatially discrete structural references during model development and evaluation. LiDAR observations are therefore not required as inference-time inputs.

Before sample extraction, Sentinel-2 imagery was processed in the WGS 84/UTM projected coordinate system of the corresponding image tiles, and all structural references were aligned to the same raster grid. GEDI footprint coordinates were transformed to Sentinel-2 pixel locations using the affine transformation of the corresponding image. For GEDI, each valid footprint was associated with the 10-m Sentinel-2 grid cell containing its centroid, and a $15 \times 15 \times 12$ Sentinel-2 patch centered on that cell was extracted as the model input. The corresponding GEDI-derived canopy height was assigned as the regression reference for the central target pixel. Each patch retained only this single-GEDI footprint as its supervisory target; GEDI observations were not duplicated as labels across multiple samples. This centroid-based association defines the supervision location but does not imply identical spatial support between the approximately 25-m GEDI footprint and the 10-m Sentinel-2 pixel. UAV- and airborne-LiDAR references were derived from ground-relative, height-normalized point clouds and rasterized to the corresponding Sentinel-2 grid before sample extraction, whereas forest-inventory measurements were retained as an independent cross-scale evaluation source.

In total, nearly 20 million GEDI footprints across the four regional domains and approximately 5.8 million UAV- and airborne-LiDAR-derived samples from 27 sites provided structural references. This framework transfers geographically distributed 3-D forest-structure information to spatially continuous optical-image regression while preserving a clear distinction between model inputs and supervision/reference data. During wall-to-wall inference, only Sentinel-2 imagery is required.

B. PRFXeption Network

1) Problem Formulation and Design Principles: Canopy-height estimation was formulated as a patch-to-pixel regression problem. For each target location p, a 15×15 Sentinel-2 patch containing 12 spectral bands was centered on the corresponding 10-m pixel

$$\mathbf{X}_p \in \mathbb{R}^{15\times 15\times 12} \tag{1}$$

where $\mathbf{X}_p$ was associated with a scalar LiDAR-derived canopy-height reference h_p. PRFXeption learns the nonlinear mapping

$$\hat{h}_p = f_{\boldsymbol{\theta}}\left(\mathbf{X}_p\right) \tag{2}$$

where $\hat{h}_p \in \mathbb{R}$ is the predicted canopy height of the central pixel and $\boldsymbol{\theta}$ denotes the trainable parameters. Thus, the task is continuous regression rather than semantic segmentation or image classification. Sentinel-2 imagery provides the model inputs, whereas canopy heights derived from GEDI, UAV LiDAR, and airborne LiDAR serve as sparse reference labels during training and evaluation.

The 15×15 neighborhood covers approximately 150×150 m and provides contextual information on crown texture, shadow patterns, canopy continuity, and stand organization that is unavailable from the central pixel alone. Such context is particularly important for detecting localized extreme-height canopies embedded within heterogeneous forest mosaics.

PRFXeption combines pyramid receptive fields with depthwise-separable convolution. A depthwise-separable convolution decomposes spatial filtering and cross-channel integration into a depthwise convolution and a 1×1 pointwise convolution, respectively, reducing model complexity while retaining spectral–spatial representation capability [36].

Parallel branches with kernel sizes of 1×1, 3×3, 5×5, and 7×7 capture complementary spatial supports [37], [38], [39]. The 1×1 branch emphasizes pixel-level

[3]Sentinel-2 data are available from the Copernicus Data Space: https://dataspace.copernicus.eu/

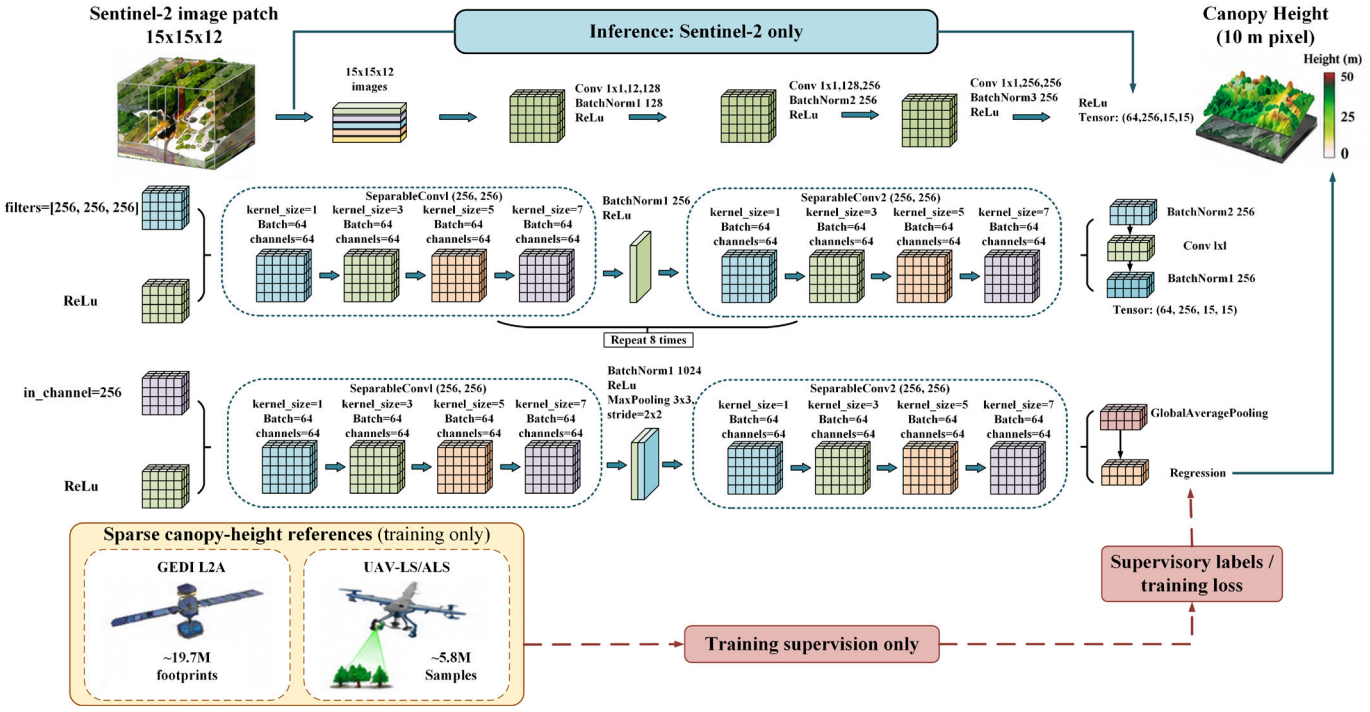


Fig. 2. PRFXeption architecture and sparse-supervision workflow. Sentinel-2 patches are the only network inputs; GEDI L2A and UAV-LS/ALS provide canopy-height references during training, whereas inference uses Sentinel-2 only.

spectral relationships, whereas the larger kernels progressively incorporate local crown-scale and broader stand-level context. This multiscale design was intended to balance average regression accuracy with sensitivity to rare extreme-height canopies rather than to assume that a single receptive field is optimal across all regions.

For an input feature tensor $\mathbf{F}$, the response of branch k is

$$\mathbf{Z}_k = \mathrm{PWConv}_k\left[\mathrm{DWConv}_k\left(\mathbf{F}\right)\right], \qquad k \in \mathcal{K} \tag{3}$$

where $\mathcal{K} = \{1, 3, 5, 7\}$, DWConv_k denotes a depthwise convolution with a $k \times k$ kernel, and PWConv_k denotes a 1×1 pointwise convolution. Each branch generates 64 feature channels, and the four outputs are concatenated as follows:

$$\mathbf{Z}_{\mathrm{cat}} = \mathrm{Concat}\left(\mathbf{Z}_1, \mathbf{Z}_3, \mathbf{Z}_5, \mathbf{Z}_7\right) \tag{4}$$

forming a 256-channel multiscale representation. The concatenated features are projected and fused with the residual input

$$\mathbf{F}' = \sigma\left\{\mathrm{BN}\left[\mathrm{Conv}_{1\times1}\left(\mathbf{Z}_{\mathrm{cat}}\right)\right] + \mathcal{P}\left(\mathbf{F}\right)\right\} \tag{5}$$

where BN denotes the batch normalization, σ is the rectified linear unit, and $\mathcal{P}$ is an identity mapping or a 1×1 projection used to align the input and output channel dimensions. The block therefore integrates multiscale spatial responses while maintaining a 256-channel feature representation.

2) Architecture of PRFXeption: The PRFXeption architecture consists of three principal components: the entry flow, middle flow, and exit flow (see Fig. 2). These components progressively transform the 12-band Sentinel-2 input into a compact contextual representation for central-pixel canopy-height regression. Multiple receptive-field sizes are used to enrich the extracted spectral and spatial features [40].

For a mini-batch containing B samples, the input tensor is arranged as follows:

$$\mathbf{X} \in \mathbb{R}^{B\times12\times15\times15} \tag{6}$$

where B is the mini-batch size, 12 is the number of Sentinel-2 bands, and 15×15 is the spatial dimension of each input patch.

The entry flow projects the input spectral channels into a higher dimensional feature space. The first 1×1 convolutional maps the 12 input bands to 128 feature channels. Batch normalization and a rectified linear unit (ReLU) activation are then applied [41], [42]. Two subsequent 1×1 convolutions expand and refine the representation to 256 channels. Batch normalization and nonlinear activation are applied between the projections, and a residual connection preserves information from the preceding feature representation [43]. The entry flow output has dimensions

$$\mathbf{F}_{\mathrm{entry}} \in \mathbb{R}^{B\times256\times15\times15}. \tag{7}$$

The middle flow consists of eight repeated residual pyramid-receptive-field blocks. Each block contains two successive multibranch depthwise-separable convolutional stages. Within each stage, the 1×1, 3×3, 5×5, and 7×7 branches each generate 64 feature channels. The four branch outputs are concatenated to form a 256-channel tensor. After the first multibranch stage, batch normalization and ReLU activation are applied. The second multibranch stage further refines the multiscale representation, after which a 1×1 convolutional projects the features to 256 channels. The projected features are normalized and added to the block input through a residual connection.

No spatial downsampling is applied in the middle flow. Consequently, the feature tensor remains

$$\mathbf{F}_{\text{middle}} \in \mathbb{R}^{B\times 256\times 15\times 15} \tag{8}$$

throughout the eight repeated blocks. Maintaining the original patch resolution allows the network to preserve spatial variation surrounding the target pixel while progressively increasing the effective receptive field [44].

The exit flow converts the spatial feature tensor into a compact regression representation [45]. An additional pyramid-receptive-field block first integrates the multiscale features inherited from the middle flow. A 3×3 max-pooling operation with a stride of two then reduces the spatial dimensions and increases the effective contextual support. A second multiscale depthwise-separable convolutional block refines the downsampled representation and projects it to 256 output channels.

Global average pooling is subsequently applied across the remaining spatial dimensions [46]

$$\mathbf{g}_p = \text{GAP}\left(\mathbf{F}_{\text{exit},p}\right), \qquad \mathbf{g}_p \in \mathbb{R}^{256} \tag{9}$$

where $\mathbf{g}_p$ is the contextual feature vector associated with target location p. A fully connected regression layer maps this vector to one continuous canopy-height estimate

$$\hat{h}_p = \mathbf{w}^{\mathrm{T}}\mathbf{g}_p + b \tag{10}$$

where $\mathbf{w} \in \mathbb{R}^{256}$ and b are the parameters of the regression head. The output is a scalar representing the predicted canopy height of the central 10-m pixel, rather than a categorical label or a spatially continuous segmentation map.

During wall-to-wall inference, a $15 \times 15 \times 12$ window is centered sequentially on each valid Sentinel-2 pixel using a 1-pixel stride. The scalar prediction produced for each input patch is assigned to its central pixel, and the resulting predictions are reassembled according to their original spatial coordinates to generate the continuous canopy-height map at 10-m resolution.

C. Sparse Supervised Training and Prediction Calibration

PRFXeption was trained under sparse supervision because canopy-height references were available only at GEDI footprints and locations covered by UAV or airborne LiDAR, whereas Sentinel-2 imagery was spatially continuous [47], [48]. Let Ω be the set of samples with valid LiDAR-derived canopy-height references, and let $\hat{h}_i$ and h_i be the predicted and reference heights for sample i, respectively. Across the four regional domains, approximately 25.5 million LiDAR-derived reference samples correspond to a nominal supervision density of about 0.28% relative to the underlying 10-m Sentinel-2 grid. This value characterizes regional-domain label sparsity rather than the exact post-masking training-pixel density. The initial training stage minimized mean squared error with L_2 regularization

$$\mathcal{L}_{\text{base}} = \frac{1}{|\Omega|}\sum_{i\in\Omega}\left(\hat{h}_i - h_i\right)^2 + \lambda\,\|\boldsymbol{\theta}\|_2^2 \tag{11}$$

where $\boldsymbol{\theta}$ denotes the trainable parameters and $\lambda = 1 \times 10^{-4}$. The network was optimized using Adam with an initial learning rate of 10^{-3} [49]; the learning rate was reduced according to validation loss. Gradient clipping used a maximum norm of 5.0, and the mini-batch size was five patches.

Preliminary validation indicated regression toward the dominant intermediate-height range, with underestimation of the tallest canopies [50]. The models were therefore retrained using height-balanced sampling, region-balanced batches, and an upper tail-aware weighted objective

$$\mathcal{L}_{\text{tail}} = \frac{1}{\sum_{i\in\Omega} w_i}\sum_{i\in\Omega} w_i\left(\hat{h}_i - h_i\right)^2 + \lambda\,\|\boldsymbol{\theta}\|_2^2 \tag{12}$$

where

$$w_i = \begin{cases} 1, & h_i < 50\ \text{m} \\ 2, & 50\ \text{m} \le h_i < 60\ \text{m} \\ 4, & h_i \ge 60\ \text{m}. \end{cases} \tag{13}$$

During upper tail retraining, the four regional domains were sampled with equal probability ($p = 0.25$), and the three height strata (<50, 50–60, and ≥ 60 m) were also sampled with equal probability ($p = 1/3$). A training sample was then randomly drawn from the selected region–height stratum, so balancing was achieved in expectation rather than by enforcing an exact mini-batch composition. All sampling, weighting, hyperparameter, architecture, and checkpoint decisions were based only on the training and validation subsets.

After the final architecture and checkpoint were fixed, a single-global affine calibration was estimated from the pooled validation predictions

$$\hat{h}^{\text{cal}} = \alpha\hat{h} + \beta \tag{14}$$

where α and β were obtained exclusively from the validation data and then frozen for independent testing and wall-to-wall prediction.

The complete workflow was therefore initial training → height- and region-balanced upper tail retraining → validation-based architecture and checkpoint selection → validation-only calibration → parameter freezing → independent testing → wall-to-wall prediction. Independent test observations were not used for optimization, model selection, loss-weight determination, sampling design, or prediction calibration.

D. Model Evaluation and Task-Oriented Model Selection

The model evaluation was designed to distinguish general canopy-height accuracy from fidelity in the sparsely represented upper tail of the canopy-height distribution. Full-distribution metrics quantified average regression performance, whereas height-stratified metrics assessed whether the model retained exceptionally tall canopies without compressing them toward the dominant intermediate-height range. This distinction was necessary because the primary objective of the resulting maps was not only general canopy-height estimation but also the screening of landscapes that may contain giant trees.

1) Overall and Upper Tail Evaluation: The coefficient of determination (R^2) was additionally calculated as a complementary goodness-of-fit metric and interpreted together with root-mean-squared error (RMSE), mean absolute error (MAE), and mean error (ME)

$$\mathrm{RMSE} = \sqrt{\frac{1}{N}\sum_{i=1}^{N}\left(\hat{h}_i - h_i\right)^2} \tag{15}$$

$$\mathrm{MAE} = \frac{1}{N}\sum_{i=1}^{N}\left|\hat{h}_i - h_i\right| \tag{16}$$

$$\mathrm{ME} = \frac{1}{N}\sum_{i=1}^{N}\left(\hat{h}_i - h_i\right) \tag{17}$$

where N is the number of reference observations, $\hat{h}_i$ is the calibrated canopy-height prediction, and h_i is the corresponding reference height. RMSE emphasizes larger deviations, MAE represents the average absolute prediction error, and ME quantifies systematic bias. Under the adopted definition, positive ME indicates overall overestimation, whereas negative ME indicates overall underestimation. Upper tail accuracy was evaluated for reference canopy heights of at least 50 and 60 m. For each height threshold, the three receptive-field configurations were evaluated on a common set of valid independent test observations. The common subsets contained 25 997 observations for reference heights $\geq$ 50 m and 3162 observations for reference heights $\geq$ 60 m. Samples were assigned to the height subsets according to their reference heights. The metrics were calculated separately for GEDI, UAV or airborne LiDAR, and forest inventory references because these datasets differ in spatial support, sampling density, geolocation uncertainty, and canopy-height definition. Regional GEDI evaluations were conducted independently for the four representative test areas, whereas UAV or airborne LiDAR and forest inventory observations were used as complementary independent references. Results from these reference sources were not pooled into a single-accuracy estimate.

Before patch extraction, Sentinel-2 image tiles within each regional domain were first assigned to spatially disjoint training, validation, and independent test subsets. The $15 \times 15 \times 12$ Sentinel-2 patches were then generated separately within these predefined spatial partitions rather than randomly splitting individual GEDI footprints or pixels. Each GEDI-supervised patch retained only one footprint as the central supervisory target, and no footprint was duplicated across subsets. Independent test samples were excluded from model training, hyperparameter and checkpoint selection, loss-weight determination, and prediction calibration. This spatial-unit-first strategy was used to reduce leakage caused by spatial autocorrelation [51]. No additional geometric buffer was imposed between the predefined spatial partitions.

Because full-distribution metrics are strongly influenced by the more abundant low- and intermediate-height observations, prediction performance was additionally evaluated within the upper tail of the reference distribution. For a predefined canopy-height threshold $\tau \in \{50, 60\}$ m, the corresponding upper tail subset was defined as follows:

$$\Omega_\tau = \{i \mid h_i \geq \tau\}, \qquad \tau \in \{50, 60\}\ \mathrm{m} \tag{18}$$

where $|\Omega_\tau|$ denotes the number of reference observations exceeding threshold τ. The thresholds were used as operational height strata for progressively evaluating tall and exceptionally tall canopies rather than as universal definitions of giant trees.

Upper tail RMSE, MAE, and ME were calculated as follows:

$$\mathrm{RMSE}_{>\tau} = \sqrt{\frac{1}{|\Omega_\tau|}\sum_{i\in\Omega_\tau}\left(\hat{h}_i - h_i\right)^2} \tag{19}$$

$$\mathrm{MAE}_{>\tau} = \frac{1}{|\Omega_\tau|}\sum_{i\in\Omega_\tau}\left|\hat{h}_i - h_i\right| \tag{20}$$

and

$$\mathrm{ME}_{>\tau} = \frac{1}{|\Omega_\tau|}\sum_{i\in\Omega_\tau}\left(\hat{h}_i - h_i\right). \tag{21}$$

Negative values of $ME_{>\tau}$ indicate systematic underestimation of canopies above the specified threshold. All receptive-field configurations were evaluated on the same common independent-test samples within each height threshold to ensure direct comparability of the upper tail metrics. Upper tail statistics were reported only where the available reference support was sufficient for a meaningful comparison.

2) Receptive-Field Comparison and Model Selection: Three receptive-field configurations were compared: a pixel-oriented 1×1 configuration, a local-context 3×3 configuration, and the full parallel $1 \times 1 - 3 \times 3 - 5 \times 5 - 7 \times 7$ PRFXeption configuration. All experiments used identical Sentinel-2 spectral inputs, LiDAR-derived reference samples, data partitions, optimization settings, loss functions, and prediction–calibration procedures. Only the receptive-field configuration was varied, thereby isolating the effect of spatial context on canopy-height estimation [52].

Architecture selection was performed exclusively using the validation data [53]. Because full-distribution metrics are dominated by the more abundant low- and intermediate-height observations, full-distribution RMSE, MAE, and ME were considered jointly with the corresponding metrics calculated for reference canopies of at least 50 and 60 m. The metrics were evaluated side by side rather than combined into an arbitrary composite score.

The final architecture was selected before independent test evaluation. Model checkpoints, hyperparameters, loss weights, and prediction–calibration coefficients were determined exclusively from the training and validation data. Once estimated, the calibration coefficients were fixed and applied without further adjustment to the independent test datasets and wall-to-wall predictions. Test reference observations were reserved exclusively for final performance assessment and were not used for architecture selection, hyperparameter tuning, checkpoint selection, loss-weight determination, or prediction calibration.

IV. Results and Discussion

For clarity, the evaluation results cover three distinct settings: regional full-distribution performance of the final calibrated PRFXeption model, comparisons of receptive-field configurations under identical experimental settings,

TABLE II

ACCURACY OF THE CALIBRATED PRFXEPTION CANOPY-HEIGHT PREDICTIONS EVALUATED AGAINST GEDI OBSERVATIONS IN FOUR SPATIALLY INDEPENDENT REGIONAL TEST SUBSETS. RMSE, MAE, AND ME ARE EXPRESSED IN METERS, WITH ME DEFINED AS PREDICTED HEIGHT MINUS REFERENCE HEIGHT

Region	N	RMSE	MAE	ME	R^2
Australia (HFV)	369,632	7.86	5.75	0.23	0.41
North America (TDS)	222,016	9.35	7.04	0.28	0.43
Southeast Asia (NMG)	314,799	9.14	7.07	0.34	0.51
Southeast Tibet (RNH)	954,844	8.42	6.47	0.54	0.21

and pooled upper-tail performance of these configurations using common independent test samples. These results therefore differ in evaluation scope and aggregation. We applied satellite-based canopy-height mapping across 24 selected landscapes within four major giant-tree regions: nine in Southeast Tibet–Northwest Yunnan, five in North America, five in Australia, and five in Southeast Asia. These maps form the basis for identifying landscapes that host giant-tree communities and for quantifying their ecological and biogeographic significance.

A. Reliability of Canopy-Height Estimation

Canopy-height predictions were evaluated against three complementary reference sources: GEDI observations, UAV or airborne LiDAR data, and forest inventory measurements. These datasets differ in spatial support, sampling density, geolocation uncertainty, and canopy-height definition, thereby providing complementary assessments of prediction reliability across observational scales. GEDI-based evaluation was conducted separately using spatially independent test subsets in Australia, North America, Southeast Asia, and southeastern Tibet, whereas UAV or airborne LiDAR and forest inventory measurements provided additional independent references at finer spatial scales.

Comparisons with GEDI observations yielded regional RMSE values of 7.86–9.35 m and MAE values of 5.75–7.07 m (see Table II). The lowest RMSE was obtained in Australia (7.86 m), followed by southeastern Tibet (8.42 m), Southeast Asia (9.14 m), and North America (9.35 m). The corresponding ME values were 0.23, 0.54, 0.34, and 0.28 m, respectively. These small positive ME values indicate limited overall overestimation relative to the substantially greater sample-level dispersion represented by RMSE and MAE. The corresponding R^2 values were 0.41, 0.43, 0.51, and 0.21 for Australia, North America, Southeast Asia, and southeastern Tibet, respectively.

The density distributions in Fig. 3 were dominated by the more abundant low- and intermediate-height observations. Prediction density generally followed the increasing reference-height gradient within these ranges, whereas dispersion increased toward the extremes of the regional height distributions. Although the regional ME values were slightly positive, observations toward the upper end of the reference distributions remained predominantly below the 1:1 relationship. This apparent difference reflects a height-dependent regression pattern rather than an inconsistency in the

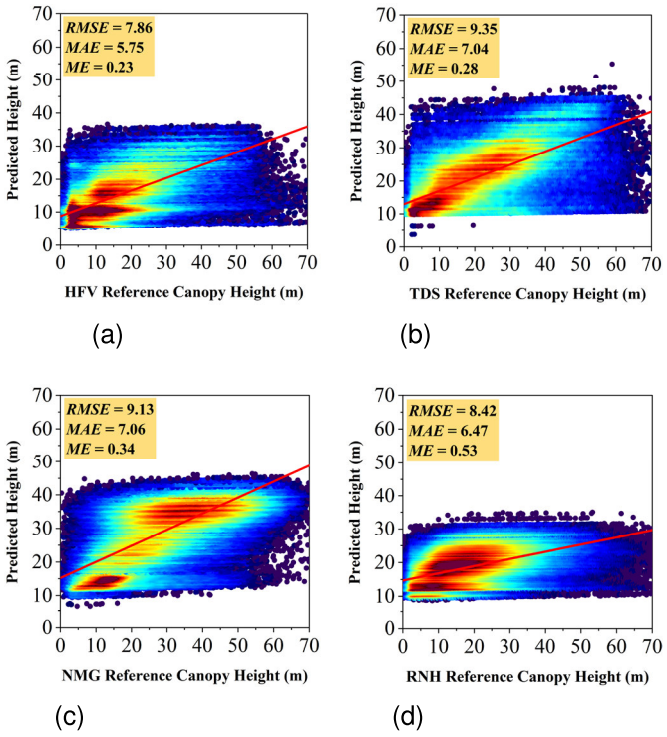


Fig. 3. Density distributions comparing the calibrated PRFXeption canopy-height predictions with GEDI reference observations in spatially independent regional test subsets. (a) Australia (HFV; N = 369 632). (b) North America (TDS; N = 222 016). (c) Southeast Asia (NMG; N = 314 799). (d) Southeastern Tibet (RNH; N = 954 844). The red line represents the 1:1 relationship. RMSE, MAE, and ME were calculated from the complete calibrated predictions in each regional test subset, with ME defined as predicted height minus reference height. The density surfaces were smoothed only for visualization and did not affect the predictions or reported accuracy statistics. The panels characterize full-distribution regional performance, whereas the pooled height-stratified performance of canopies reaching at least 50 and 60 m is evaluated separately in Table VI.

TABLE III

INDEPENDENT VALIDATION OF CANOPY-HEIGHT PREDICTIONS AGAINST UAV OR AIRBORNE LIDAR AND FOREST INVENTORY MEASUREMENTS

Reference data	RMSE (m)	MAE (m)	ME (m)	R^2
UAV/airborne LiDAR	5.19	4.05	1.46	0.41
Forest inventory	6.94	5.65	0.20	0.35

evaluation: slight overestimation among the more numerous low- and intermediate-height observations coexisted with residual underestimation among the comparatively rare tallest canopies.

The statistics reported in Fig. 3 and Table II quantify prediction performance over the complete reference-height distribution within each region. They should therefore be distinguished from the pooled height-stratified evaluation in Table VI, which includes only reference observations reaching at least 50 or 60 m. The two analyses address complementary aspects of model performance: regional full-distribution accuracy and sensitivity to the extreme upper tail, respectively.

Independent evaluation against UAV or airborne LiDAR and forest inventory measurements yielded RMSE values of 5.19 and 6.94 m, MAE values of 4.05 and 5.65 m, and R^2 values of 0.41 and 0.35, respectively (see Table III). Differences

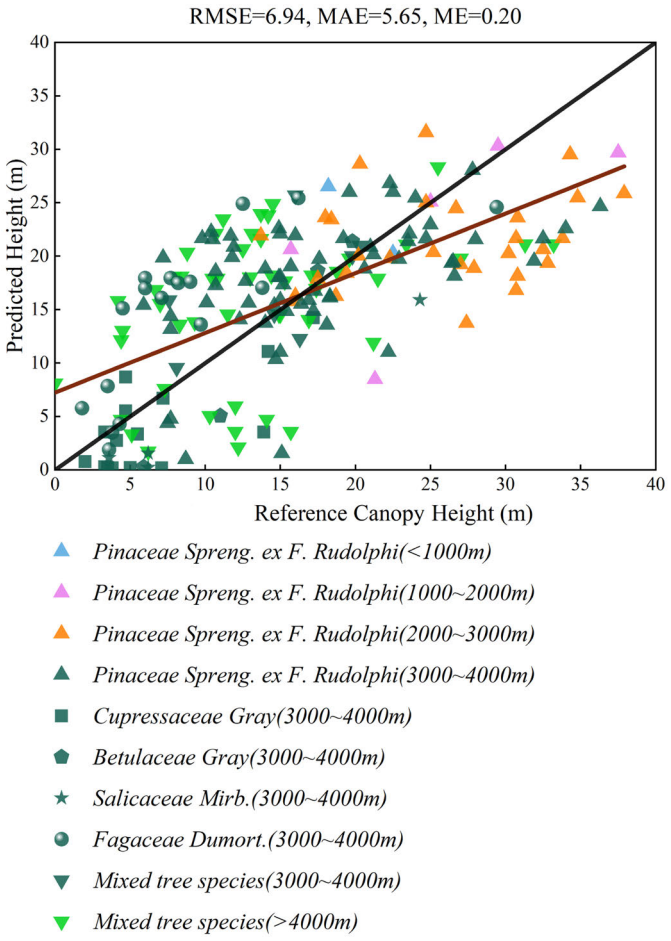


Fig. 4. Comparison of PRFXeption canopy-height predictions with forest inventory measurements in southeastern Tibet. Predictions generally follow the reference measurements, whereas dispersion increases toward the upper end of the observed canopy-height range.

among the GEDI-, UAV/airborne-LiDAR-, and field-based accuracy estimates partly reflect differences in spatial resolution, observation support, sampling design, geolocation uncertainty, and canopy-height definition among the reference datasets. Accordingly, these source-specific metrics were interpreted separately rather than pooled into a single-accuracy estimate.

The field-based comparison in southeastern Tibet produced an ME of 0.20 m, indicating little overall systematic bias, although substantial sample-level dispersion remained (see Fig. 4). Predictions generally followed the reference measurements across the observed height range, but dispersion increased for taller forest plots, and the upper end of the height distribution showed a tendency toward underestimation. These results are consistent with the height-dependent error pattern observed in the GEDI-based regional evaluations.

Terrain exerted a clear influence on prediction accuracy (see Fig. 5). Errors remained relatively stable over gentle terrain but generally increased as slopes became steeper. The most pronounced deterioration occurred in southeastern Tibet, where complex topography can increase uncertainty in ground-elevation retrieval, LiDAR footprint positioning, and the spatial correspondence between GEDI observations and

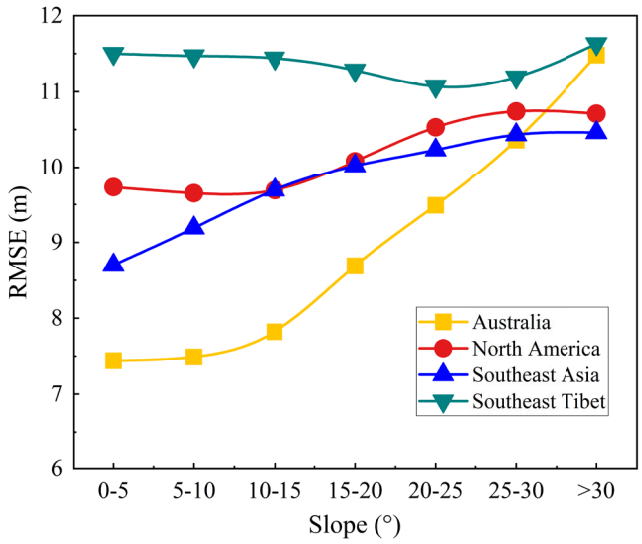


Fig. 5. Relationship between canopy-height prediction accuracy and terrain slope. RMSE remains relatively stable over gentle terrain but generally increases with slope, with the most pronounced deterioration occurring in southeastern Tibet.

Sentinel-2 pixels [54], [55]. The increase in RMSE on slopes exceeding approximately 30° indicates that terrain-related uncertainty remains an important limitation for canopy-height estimation in mountainous giant-tree regions.

To further assess the spatial plausibility of the predictions, the PRFXeption canopy-height maps were compared with the Global Forest Watch canopy-height product [13], [56], the 30-m canopy-height map of China [6], and high-resolution optical imagery (see Fig. 6). The PRFXeption maps preserved finer spatial variation and more localized tall-canopy patterns within the evaluated landscapes, including features that corresponded more closely to forest textures visible in the high-resolution imagery. However, because the compared products differ in spatial resolution, acquisition period, input data, and modeling strategy, these comparisons were interpreted primarily as qualitative assessments of spatial detail rather than as additional quantitative validation of prediction accuracy.

B. Spectral-Input and Receptive-Field Effects

Controlled ablation experiments were conducted to examine how Sentinel-2 spectral composition and receptive-field support affected canopy-height prediction. The spectral-input experiments compared five configurations: the 10-m near-infrared band (B08), the 10-m red–green–blue bands (RGB; B02–B04), the combined 10-m RGB and near-infrared bands (RGBN; B02–B04, and B08), the bands acquired at native spatial resolutions of 20 or 60 m (B01, B05–B07, B8A, and B09–B12), and all 13 Sentinel-2 bands. Within this ablation, only the spectral inputs were changed, while the reference samples, data partitions, network configuration, and optimization settings were held constant.

The spectral-input ablation showed that no single-band combination achieved the lowest error in all regions (see

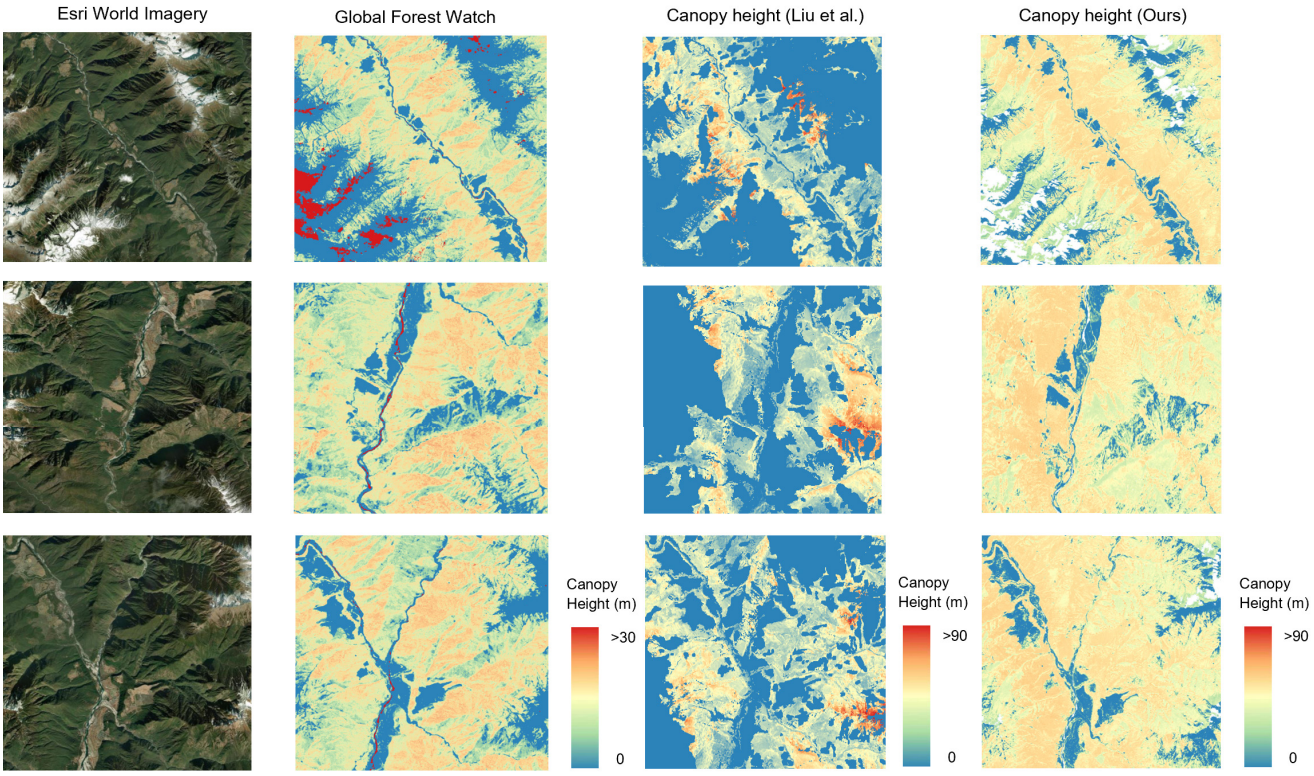


Fig. 6. Qualitative comparison of canopy-height products and high-resolution optical imagery in Southeast Tibet. The PRFXeption maps preserve finer spatial variation and more distinct tall-canopy patterns than the compared canopy-height products. Differences in spatial resolution, acquisition period, and modeling strategy should be considered when interpreting the comparison.

TABLE IV
DIAGNOSTIC SPECTRAL-INPUT ABLATION CONDUCTED UNDER THE EARLIER 13-BAND SENTINEL-2 CONFIGURATION. THESE EXPERIMENTS ASSESS SPECTRAL-COMPOSITION AND NATIVE-RESOLUTION EFFECTS AND WERE NOT USED AS DIRECT EVIDENCE FOR SELECTING THE FINAL 12-BAND INPUT

		N	RGB	RGBN	woRGBN	All bands
Australia (HEV)	RMSE	10.45	11.58	11.17	11.83	15.04
	MAE	7.89	8.71	8.26	8.73	11.82
	ME	-1.30	-5.30	-4.11	-5.46	-10.41
North America (TDL)	RMSE	10.75	10.89	10.68	10.88	12.22
	MAE	8.40	8.30	8.12	8.22	9.19
	ME	0.04	-1.45	-0.96	-1.99	-5.27
Southeast Asia (NLJ)	RMSE	9.58	9.55	9.39	9.32	9.74
	MAE	7.61	7.57	7.45	7.38	7.66
	ME	0.07	-1.09	-1.08	-0.42	-1.90
Southeast Tibet-Northwest Yunnan (RFT)	RMSE	12.97	13.02	13.24	13.40	13.81
	MAE	10.08	10.08	10.26	10.42	11.10
	ME	-4.11	-4.36	-3.96	-3.89	-1.17

Table IV). The B08-only configuration yielded the lowest RMSE in Australia and southeastern Tibet–northwestern Yunnan, with values of 10.45 and 12.97 m, respectively. The RGBN configuration performed best in North America, where it produced an RMSE of 10.68 m and an MAE of 8.12 m. In Southeast Asia, the 20-/60-m configuration achieved the lowest RMSE and MAE, with values of 9.32 and 7.38 m, respectively. These regional differences indicate that the contribution of individual spectral domains varied with forest composition, canopy architecture, terrain, and image-acquisition conditions.

The 13-band configuration produced the highest RMSE in all four regions, reaching 15.04 m in Australia, 12.22 m in North America, 9.74 m in Southeast Asia, and 13.81 m in southeastern Tibet–northwestern Yunnan. Increasing spectral dimensionality therefore did not consistently improve canopy-height estimation. The competitive performance of the 10-m B08 and RGBN configurations indicates that spatially detailed spectral and textural information was important for representing crown boundaries, shadows, and local canopy transitions. The bands acquired at native resolutions of 20 or 60 m provided complementary spectral information, but their resampling to 10 m did not restore the spatial detail available in the native 10-m observations.

The reference–prediction comparisons in Fig. 7 further illustrate the spectral-input effects. Predicted canopy-height ranges were generally narrower than the corresponding reference ranges, indicating compression of the height distribution toward its more densely represented intermediate portion. The magnitude of this compression differed between band configurations and regions. B08-based predictions generally retained a relatively broad height range in Australia and southeastern Tibet–northwestern Yunnan, consistent with their lower regional RMSE values. However, the regionally varying rankings demonstrate that near-infrared information alone was not universally optimal.

The spectral ablation was conducted under an earlier 13-band experimental configuration. Because the 13-band and 20-/60-m configurations included the Sentinel-2 cirrus band

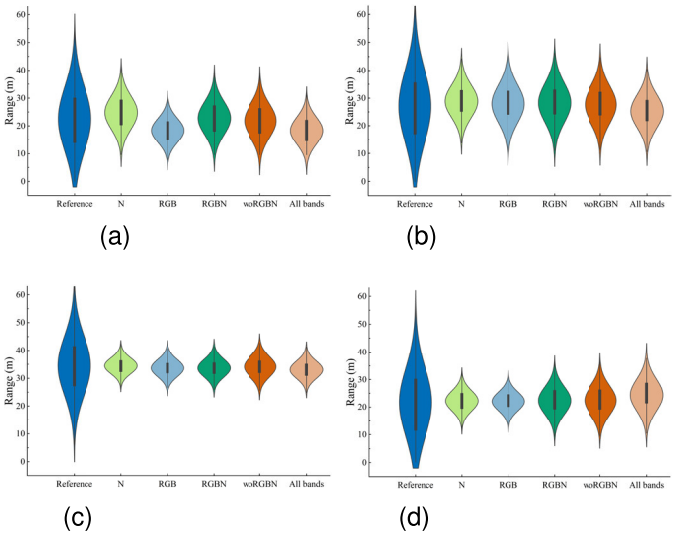


Fig. 7. Comparison of reference and predicted canopy heights obtained using different Sentinel-2 spectral-input configurations in the four giant-tree regions. Predicted height ranges were generally narrower than the corresponding reference ranges, although the degree of distributional compression varied between spectral configurations and regions. (a) Australia. (b) North America. (c) Southeast Asia. (d) Southeast Tibet.

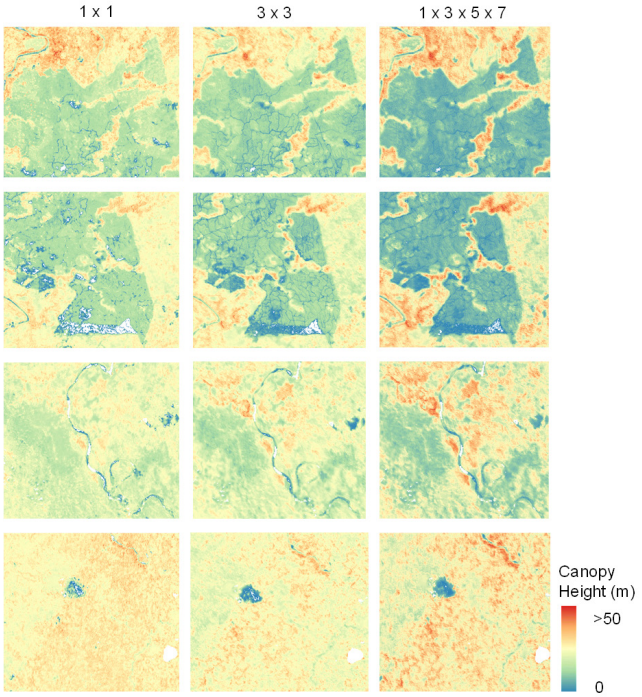


Fig. 8. Qualitative comparison of canopy-height maps generated using different receptive-field configurations. The 1 × 1 configuration primarily represents pixel-level spectral relationships, the 3 × 3 configuration incorporates local neighborhood information, and the multiscale PRFXeption configuration combines local crown-scale responses with broader stand-level context. Quantitative full-distribution performance is reported in Table V.

TABLE V

OVERALL CANOPY-HEIGHT PREDICTION ACCURACY OBTAINED USING DIFFERENT RECEPTIVE-FIELD CONFIGURATIONS. RMSE, MAE, AND ME ARE EXPRESSED IN METERS. BOLD VALUES INDICATE THE LOWEST RMSE AND MAE WITHIN EACH REGION. ME WAS DEFINED AS PREDICTED HEIGHT MINUS REFERENCE HEIGHT; NEGATIVE VALUES THEREFORE INDICATE OVERALL UNDERESTIMATION

Region	Receptive-field configuration	RMSE	MAE	ME
Australia	1 × 1	8.33	5.88	-3.02
	3 × 3	8.05	5.64	-3.30
	1 × 3 × 5 × 7	12.91	9.77	-9.52
North America	1 × 1	9.58	7.11	-0.35
	3 × 3	9.11	6.58	-0.43
	1 × 3 × 5 × 7	9.27	6.77	-0.24
Southeast Asia	1 × 1	9.42	7.06	-0.22
	3 × 3	9.19	6.89	-0.23
	1 × 3 × 5 × 7	9.22	6.92	-0.82
Southeast Tibet-Northwest Yunnan	1 × 1	8.02	6.09	-1.70
	3 × 3	7.94	6.00	-2.02
	1 × 3 × 5 × 7	8.09	6.10	-2.56

B10, they should not be interpreted as direct evaluations of the final PRFXeption input. The final model excluded B10 and used the remaining 12 Sentinel-2 bands after resampling the 20- and 60-m observations to 10 m. The spectral results therefore provide diagnostic evidence of band-combination and native-resolution effects rather than a direct comparison between the final 12-band model and a single-band alternative.

The contribution of spatial context was examined by comparing three receptive-field configurations: a pixel-oriented 1 × 1 model, a local-context 3 × 3 model, and the parallel 1 × 3 × 5 × 7 configuration used in PRFXeption. Only the receptive-field configuration was varied, while the spectral inputs, reference samples, data partitions, and optimization settings were held constant. The corresponding full-distribution RMSE, MAE, and ME values are reported in Table V.

The 3 × 3 configuration achieved the lowest full-distribution RMSE and MAE in all four regions (see Table V). The multiscale configuration yielded broadly comparable errors in North America, Southeast Asia, and southeastern Tibet–northwestern Yunnan, with RMSE increases of only 0.16, 0.03, and 0.15 m, respectively. In contrast, performance degraded markedly in Australia, where RMSE/MAE increased from 8.05/5.64 to 12.91/9.77 m, and ME shifted from −3.30 to −9.52 m. These results show that broader spatial context is region-dependent and does not consistently improve average canopy-height regression; therefore, the multiscale configuration should not be interpreted as universally superior.

The spatial consequences of receptive-field configuration are illustrated in Fig. 8. The 1 × 1 model relied primarily on pixel-level spectral relationships and produced comparatively fragmented spatial patterns. The 3 × 3 configuration incorporated local neighborhood information and generated more coherent crown-scale variation. The multiscale configuration combined local responses with broader spatial context and qualitatively retained localized high-canopy patches together with stand-level spatial continuity.

The quantitative and qualitative comparisons provide complementary but distinct evidence. The 3 × 3 configuration was preferable when model selection was based solely on full-distribution RMSE and MAE. The multiscale configuration did not achieve the lowest average error, but it provided a unified representation of pixel-, crown-, and stand-level spatial context and qualitatively preserved localized tall-canopy patterns in the resulting maps.

TABLE VI

POOLED UPPER TAIL ACCURACY OF THE RETRAINED RECEPTIVE-FIELD CONFIGURATIONS EVALUATED ON THE SAME COMMON SET OF VALID INDEPENDENT TEST OBSERVATIONS WITHIN EACH HEIGHT THRESHOLD AFTER VALIDATION-ONLY CALIBRATION. RMSE, MAE, AND ME ARE EXPRESSED IN METERS; NEGATIVE ME INDICATES RESIDUAL UNDERESTIMATION

Receptive-field configuration	Reference-height subset	RMSE	MAE	ME
1×1	≥ 50 m	9.72	7.58	−2.86
	≥ 60 m	10.93	8.61	−4.03
3×3	≥ 50 m	9.26	7.09	−2.14
	≥ 60 m	10.61	8.17	−3.35
$1 \times 3 \times 5 \times 7$	≥ 50 m	8.68	6.54	−1.46
	≥ 60 m	10.18	7.74	−2.62

The height-stratified evaluation provided quantitative evidence for the upper-tail performance of the three receptive-field configurations (see Table VI). For reference canopies of at least 50 m, RMSE values were 9.72, 9.26, and 8.68 m for the 1×1, 3×3, and multiscale configurations, respectively. For canopies of at least 60 m, the corresponding RMSE values were 10.93, 10.61, and 10.18 m. The multiscale configuration also achieved the lowest MAE and the smallest magnitude of ME at both thresholds. The spatial patterns shown in Fig. 8 are consistent with these quantitative results, indicating that broader spatial context helped retain coherent high-canopy features. Its practical utility was further evaluated through wall-to-wall mapping and UAV-based confirmation of candidate giant-tree communities.

Overall, the ablation experiments indicate that increasing spectral dimensionality or receptive-field size does not consistently improve canopy-height prediction across all regions. The 3×3 configuration was more effective for minimizing full-distribution regression error, whereas the multiscale configuration showed lower errors in the pooled ≥50- and ≥60-m independent test subsets, reflecting a task-dependent benefit of broader spatial context for extreme-height canopies. The multiscale configuration used for wall-to-wall mapping was selected exclusively from validation results before independent testing; accordingly, Table VI provides independent confirmation of its upper tail behavior rather than evidence used for architecture selection.

The regional full-distribution evaluation and the pooled height-stratified evaluation provide complementary evidence of model performance. Fig. 3 and Table II report the accuracy of the selected multiscale model separately over the complete reference-height distribution of each region. In contrast, Table VI lists the comparison of the three receptive-field configurations using only pooled independent test observations whose reference canopy heights reached the predefined 50- and 60-m thresholds. The resulting metrics therefore represent different height ranges, aggregation schemes, and evaluation objectives and are not directly interchangeable.

C. Continuous Mapping of Giant-Tree Landscapes

Following spatially independent evaluation, the calibrated PRFXeption model was applied to the 24 selected landscapes to generate continuous canopy-height maps at 10-m resolution. The source-dependent RMSE values were 7.86–9.35 m across the four GEDI-based regional test subsets, 5.19 m against UAV or airborne LiDAR, and 6.94 m against forest inventory measurements (see Tables II and III). These results support the use of the maps for regional screening of unusually tall forest landscapes. However, because each prediction represents canopy height associated with a 10-m pixel, individual high-value pixels should be interpreted as candidate tall-canopy locations rather than as direct measurements of individual giant trees.

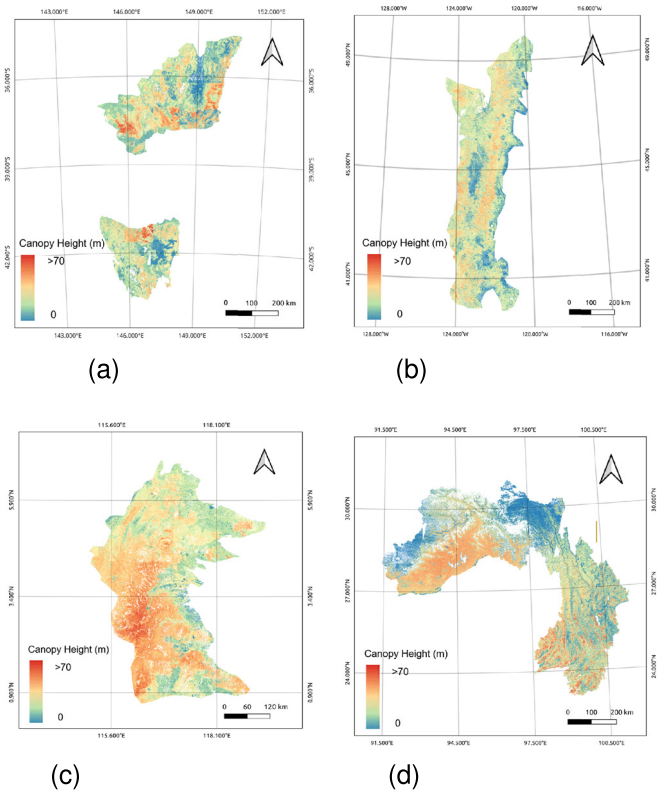


Fig. 9. Continuous 10-m canopy-height predictions for the 24 selected landscapes grouped into (a) southeastern Australia, (b) northwestern North America, (c) Southeast Asia, and (d) southeastern Tibet–northwestern Yunnan. Warmer colors indicate taller predicted canopies. The maps are intended for regional landscape screening; individual high-value pixels should not be interpreted as direct measurements of individual tree height.

The resulting maps revealed substantial spatial variation within and among the selected landscapes (see Fig. 9). Spatially coherent patches with predicted canopy heights above 35 m were particularly evident in southeastern Tibet–northwestern Yunnan and Southeast Asia, whereas high-canopy patches appeared more spatially discrete within the selected landscapes of southeastern Australia and northwestern North America. These comparisons describe the mapped spatial patterns rather than the regional abundance of giant trees because the analyzed extents, environmental conditions, and reference-data coverage differed among regions.

Localized valley-associated patches in southeastern Tibet–northwestern Yunnan contained high-ranked candidate pixels whose calibrated predictions exceeded 70 m. These values were used for candidate ranking rather than as direct

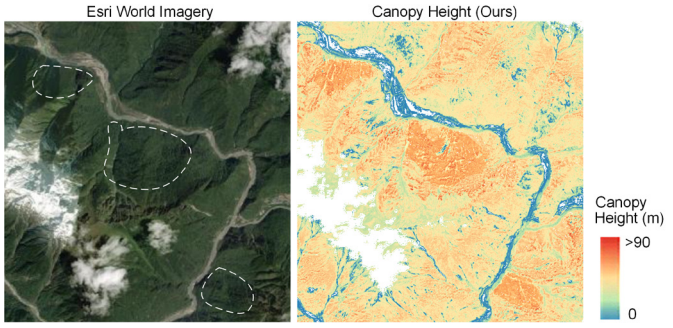


Fig. 10. Candidate giant-tree sites identified by combining canopy-height maps with high-resolution imagery. (Top and bottom) Circles highlight the previously documented site (middle) and two additional candidate sites.

estimates of individual tree height. Given the remaining uncertainty in the extreme upper tail and the increased prediction error in steep terrain, these values should be regarded as indicators of locations requiring high-resolution confirmation. The continuous maps therefore provide a spatial screening layer that narrows the search area for targeted UAV LiDAR and field surveys while revealing tall-canopy patterns that cannot be resolved from spatially discontinuous GEDI observations alone.

D. From Canopy Maps to Giant-Tree Discovery

The practical value of the continuous canopy-height maps was evaluated through a satellite-guided screening and confirmation workflow. Spatially coherent high-canopy patches were first identified from the 10-m PRFXeption predictions and then examined together with high-resolution optical imagery. The optical data were used to verify that the predicted patterns corresponded to continuous forest cover and to exclude obvious nonforest features or isolated mapping artifacts.

This screening recovered the spatial pattern associated with a previously documented giant-tree community along the Yigong Tsangpo River [5], [26] and highlighted two additional candidate sites that were not represented in the available field records (see Fig. 10). Subsequent UAV LiDAR surveys confirmed trees taller than 60 m at both candidate sites, including trees exceeding 70 m at one site. These observations confirmed that the screened high-canopy patterns corresponded to tall-forest areas rather than isolated anomalous pixels.

These results demonstrate that continuous 10-m canopy-height mapping can substantially reduce the search area for giant-tree investigation. The predicted maps do not directly identify or measure individual giant trees; instead, they provide a regional screening layer for prioritizing spatially coherent candidate landscapes for subsequent UAV LiDAR and field verification. The resulting workflow links spatially continuous satellite prediction with targeted high-resolution structural confirmation, supporting satellite-guided screening of candidate giant-tree landscapes.

E. Implications for Carbon and Biodiversity

The predicted canopy-height maps were qualitatively compared with independent aboveground-biomass and

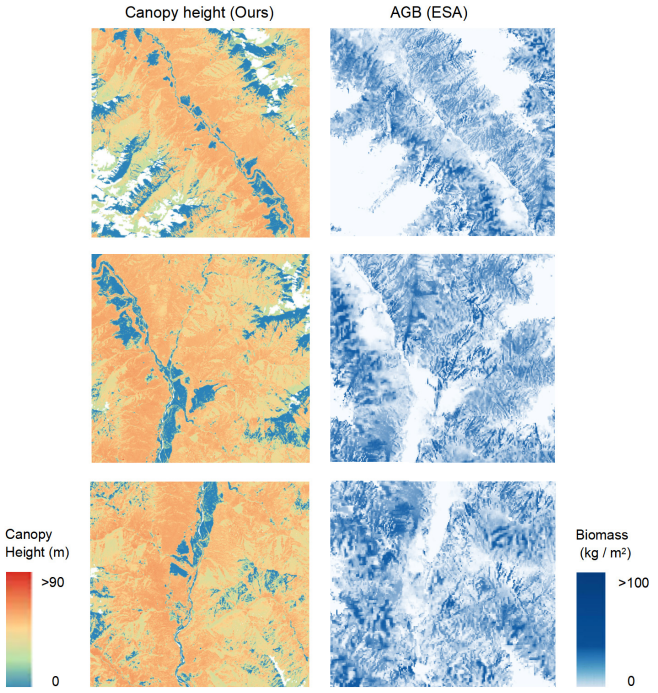


Fig. 11. Qualitative spatial comparison between predicted canopy height and an independent aboveground-biomass layer in selected giant-tree landscapes. Similar spatial patterns indicate descriptive co-occurrence between tall canopy and high biomass but do not constitute pixel-level validation or a direct estimate of carbon storage.

biodiversity-integrity layers to examine the ecological context of the mapped tall-canopy landscapes. In the selected examples, areas of taller predicted canopy frequently coincided with areas of relatively high-aboveground biomass (see Fig. 11). This spatial correspondence is ecologically plausible because canopy height and biomass both reflect aspects of stand development and structural accumulation [57]. However, the comparison is descriptive because the two products differ in spatial resolution, acquisition period, measurement definition, and modeling uncertainty. Accordingly, the PRFXeption maps provide complementary information on forest vertical structure but do not directly estimate biomass or carbon density.

Forest vertical structure also contributes to habitat heterogeneity and is often associated with greater species and functional diversity [58]. Some mapped tall-canopy patterns overlapped with areas of relatively high biodiversity integrity (see Fig. 12). Nevertheless, canopy height is not a direct proxy for biodiversity, which also depends on species composition, habitat connectivity, disturbance history, climate, topography, and management. The canopy-height maps should therefore be interpreted as complementary structural information for prioritizing landscapes that warrant integrated biodiversity and field-based ecological assessment.

Together, these comparisons indicate that continuous canopy-height maps can complement independent biomass and biodiversity datasets by providing spatially explicit information on forest vertical structure. Their principal ecological value lies in prioritizing structurally exceptional forests for

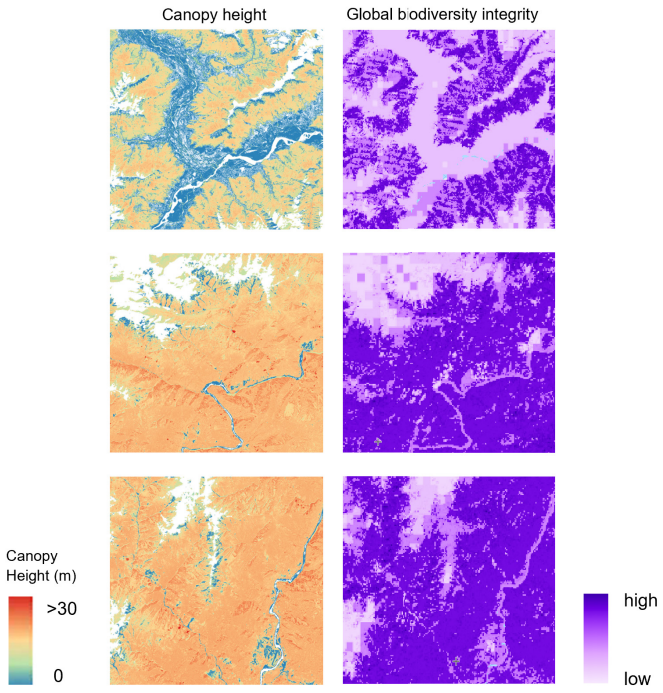


Fig. 12. Qualitative spatial comparison between predicted canopy height and the biodiversity-integrity layer used in this study. Some tall-canopy patterns coincide with areas of relatively high biodiversity integrity; the comparison provides ecological context rather than evidence that canopy height is a direct proxy for biodiversity.

targeted carbon assessment, biodiversity surveys, and conservation planning.

F. Limitations and Outlook

Several limitations constrain the interpretation and broader application of the resulting canopy-height maps. The extreme upper tail of the reference distribution remained sparsely represented, causing the tallest canopies to be compressed toward the dominant intermediate-height range. The maps are therefore suitable for identifying candidate tall-canopy landscapes within the evaluated regions, but individual high-value pixels should not be interpreted as precise measurements of individual giant trees.

Prediction uncertainty increased in steep terrain, particularly on slopes exceeding approximately 30°. Potential sources of terrain-related error include uncertainty in ground-elevation retrieval, LiDAR geolocation, topographic illumination, and the spatial correspondence between GEDI footprints and 10-m Sentinel-2 pixels. Differences in spatial support, acquisition date, and canopy-height definition among GEDI, UAV or airborne LiDAR, forest inventory, and Sentinel-2 observations introduce additional uncertainty.

The model was developed and evaluated within selected landscapes representing four major giant-tree regions. Its performance should therefore not be assumed to transfer uniformly to forest types, disturbance regimes, or environmental conditions that were not represented in the current reference data. The comparisons with biomass and biodiversity products also provide ecological context rather than quantitative estimates of carbon storage or biodiversity.

Although the multiscale model achieved RMSE values of 8.68 and 10.18 m for reference canopies of at least 50 and 60 m, respectively, prediction uncertainty remained greater for the sparsely represented upper tail, particularly for canopies above approximately 80 m. Future research should expand reference sampling within the extreme canopy-height range, incorporate terrain-aware modeling and explicit spatial uncertainty assessment, and evaluate transferability using geographically independent regions. Integration with higher resolution optical imagery, UAV LiDAR, field inventories, disturbance history, habitat connectivity, and other ecological observations would further strengthen the confirmation and conservation assessment of giant-tree landscapes. Repeated mapping may also support disturbance and recovery monitoring, although reliable update intervals must be established through dedicated multitemporal validation.

V. Conclusion

This study developed PRFXeption, a sparse multisource LiDAR-supervised patch-to-pixel framework for continuous 10-m Sentinel-2 canopy-height mapping. Three main findings emerged. First, independent evaluations yielded RMSE values of 5.19 m against UAV/airborne LiDAR, 6.94 m against forest inventory measurements, and 7.86–9.35 m across four spatially independent GEDI regional test subsets, although errors increased on slopes above approximately 30° and the tallest canopies remained moderately underestimated. Second, receptive-field experiments revealed a task-dependent trade-off: the 3×3 configuration minimized full-distribution regression error, whereas the multiscale configuration showed better preservation of the pooled upper tail and should therefore be interpreted as a screening-oriented rather than universally superior solution. Third, the resulting maps provided a practical screening layer for spatially coherent tall-canopy landscapes. Combined with high-resolution optical imagery, they highlighted two candidate communities not represented in the field records available to this study; subsequent UAV LiDAR confirmed trees taller than 60 m at both sites, including trees exceeding 70 m at one site. The mapped patterns further support southeastern Tibet–northwestern Yunnan as a candidate fourth major global concentration of giant trees. These results demonstrate the value of sparse LiDAR-supervised optical mapping for regional canopy-height characterization and targeted investigation of rare tall-canopy landscapes.

Data Availability

The PRFXeption model code and implementation materials are available at https://ieee-dataport.org//documents/discovering-giant-treecommunities-using-lidar-and-sentinel-2-data-training-code, and the 10-m canopy-height maps and associated dataset products for the selected giant-tree landscapes are available at https://ieee-dataport.org//documents/global-giant-tree-distribution-areasdataset. GEDI, Sentinel-2, and public airborne-LiDAR data can be obtained from the repositories listed in Section II-B. Raw UAV LiDAR and forest-inventory data are available from the corresponding author upon reasonable request, subject to institutional, data-licensing, and site-protection restrictions.

ACKNOWLEDGMENT

The authors thank Prof. Qinghua Guo and his team at Peking University, Beijing, China, for discovering Asia's tallest tree, and Chinese Giant-Tree Research Team—including the Institute of Botany, Chenshan Center, China Environmental Protection Foundation, "Wild China" Studio, and Zayü County Forestry Bureau—for their invaluable contributions to the study of Chinese giant trees.

REFERENCES

[1] D. B. Lindenmayer and W. F. Laurance, "The ecology, distribution, conservation and management of large old trees," *Biol. Rev.*, vol. 92, no. 3, pp. 1434–1458, Aug. 2017.

[2] J. A. Lutz et al., "Global importance of large-diameter trees," *Global Ecol. Biogeography*, vol. 27, no. 7, pp. 849–864, 2018.

[3] N. Lang, W. Jetz, K. Schindler, and J. D. Wegner, "A high-resolution canopy height model of the Earth," *Nature Ecol. Evol.*, vol. 7, no. 11, pp. 1778–1789, Sep. 2023.

[4] R. Monastersky, "Finding the Amazon's tallest trees—An epic quest to reach hidden giants," *Nature*, vol. 618, no. 7964, pp. 228–233, Jun. 2023.

[5] Y. Ren et al., "Conserving the primary forests in the Yarlung Tsangpo grand canyon for people and nature," *Nature Ecol. Evol.*, vol. 8, no. 5, pp. 837–839, Apr. 2024.

[6] X. Liu et al., "Neural network guided interpolation for mapping canopy height of China's forests by integrating GEDI and ICESat-2 data," *Remote Sens. Environ.*, vol. 269, Feb. 2022, Art. no. 112844.

[7] M. Schwartz et al., "High-resolution canopy height map in the Landes forest (France) based on GEDI, Sentinel-1, and Sentinel-2 data with a deep learning approach," *Int. J. Appl. Earth Observ. Geoinf.*, vol. 128, Apr. 2024, Art. no. 103711.

[8] S. Oehmcke et al., "Deep point cloud regression for above-ground forest biomass estimation from airborne LiDAR," *Remote Sens. Environ.*, vol. 302, Mar. 2024, Art. no. 113968.

[9] D. B. Coyle, P. R. Stysley, F. L. Chirag, E. Frese, and D. Poulios, "The global ecosystem dynamics investigation (GEDI) LiDAR laser transmitter," *Proc. SPIE*, vol. 11128, pp. 112–125, Jul. 2019.

[10] X. Li et al., "First validation of GEDI canopy heights in African savannas," *Remote Sens. Environ.*, vol. 285, Feb. 2023, Art. no. 113402.

[11] Z. Hao et al., "Automated tree-crown and height detection in a young forest plantation using mask region-based convolutional neural network (Mask R-CNN)," *ISPRS J. Photogramm. Remote Sens.*, vol. 178, pp. 112–123, Aug. 2021.

[12] S. A. Spawn, C. C. Sullivan, T. J. Lark, and H. K. Gibbs, "Harmonized global maps of above and belowground biomass carbon density in the year 2010," *Sci. Data*, vol. 7, no. 1, p. 112, Apr. 2020.

[13] P. Potapov et al., "Mapping global forest canopy height through integration of GEDI and Landsat data," *Remote Sens. Environ.*, vol. 253, Feb. 2021, Art. no. 112165.

[14] W. Qi et al., "Mapping large-scale pantropical forest canopy height by integrating GEDI LiDAR and TanDEM-X InSAR data," *Remote Sens. Environ.*, vol. 318, Mar. 2025, Art. no. 114534.

[15] B. Fu et al., "Retrieval performance of mangrove tree heights using multiple machine learning regression models and UAV-LiDAR point clouds," *Int. J. Digit. Earth*, vol. 17, no. 1, Dec. 2024, Art. no. 2392851.

[16] B. Fu et al., "Quantifying vegetation species functional traits along hydrologic gradients in Karst wetland based on 3D mapping with UAV hyperspectral point cloud," *Remote Sens. Environ.*, vol. 307, Jun. 2024, Art. no. 114160.

[17] B. Fu et al., "Estimation of mangrove heights and aboveground biomass using UAV-LiDAR, Sentinel-1 and ZY-3 stereo images," *Ecol. Informat.*, vol. 88, Sep. 2025, Art. no. 103160.

[18] W. Li, Z. Niu, R. Shang, Y. Qin, L. Wang, and H. Chen, "High-resolution mapping of forest canopy height using machine learning by coupling ICESat-2 LiDAR with Sentinel-1, Sentinel-2 and Landsat-8 data," *Int. J. Appl. Earth Observ. Geoinf.*, vol. 92, Oct. 2020, Art. no. 102163.

[19] L. Duncanson et al., "Aboveground biomass density models for NASA's global ecosystem dynamics investigation (GEDI) LiDAR mission," *Remote Sens. Environ.*, vol. 270, Aug. 2022, Art. no. 112845.

[20] G. Matasci et al., "Large-area mapping of Canadian boreal forest cover, height, biomass and other structural attributes using Landsat composites and LiDAR plots," *Remote Sens. Environ.*, vol. 209, pp. 90–106, May 2018.

[21] R. Fischer, N. Knapp, F. Bohn, H. H. Shugart, and A. Huth, "The relevance of forest structure for biomass and productivity in temperate forests: New perspectives for remote sensing," *Surv. Geophys.*, vol. 40, no. 4, pp. 709–734, Jul. 2019.

[22] L. Ma, Y. Liu, X. Zhang, Y. Ye, G. Yin, and B. A. Johnson, "Deep learning in remote sensing applications: A meta-analysis and review," *ISPRS J. Photogramm. Remote Sens.*, vol. 152, pp. 166–177, Jun. 2019.

[23] C. Willmott and K. Matsuura, "Advantages of the mean absolute error (MAE) over the root mean square error (RMSE) in assessing average model performance," *Climate Res.*, vol. 30, pp. 79–82, May 2005.

[24] J. C. White et al., "A best practices guide for generating forest inventory attributes from airborne laser scanning data using an area-based approach," *Forestry Chronicle*, vol. 89, no. 6, pp. 722–723, Dec. 2013.

[25] A. Shenkin et al., "The World's tallest tropical tree in three dimensions," *Frontiers Forests Global Change*, vol. 2, p. 32, Jun. 2019.

[26] Y. Ren et al., "Discovering and measuring giant trees through the integration of multi-platform LiDAR data," *Methods Ecol. Evol.*, vol. 15, no. 10, pp. 1889–1905, Oct. 2024.

[27] Y. Yichou, G. Dengyi, and L. Bosheng, "A great geographical discovery in the end of 20th century demonstration on the Yarlung Zangbo River Valley as the grandest canyon in the world," *Geographical Res.*, vol. 15, no. 4, pp. 1–9, 1996.

[28] N. Qin, W. Tan, L. Ma, D. Zhang, H. Guan, and J. Li, "Deep learning for filtering the ground from ALS point clouds: A dataset, evaluations and issues," *ISPRS J. Photogramm. Remote Sens.*, vol. 202, pp. 246–261, Aug. 2023.

[29] X. Zhao, Q. Guo, Y. Su, and B. Xue, "Improved progressive TIN densification filtering algorithm for airborne LiDAR data in forested areas," *ISPRS J. Photogramm. Remote Sens.*, vol. 117, pp. 79–91, Jul. 2016.

[30] C. A. Silva et al., "rGEDI: NASA's Global Ecosystem Dynamics Investigation (GEDI) data visualization and processing," *R package*, 2020. [Online]. Available: https://CRAN.R-project.org/package=rGEDI

[31] T. Fatoyinbo et al., "The NASA AfriSAR campaign: Airborne SAR and LiDAR measurements of tropical forest structure and biomass in support of future space missions," *Remote Sens. Environ.*, vol. 264, Oct. 2022, Art. no. 112533, doi: 10.1016/j.rse.2021.112533.

[32] N. Lang, N. Kalischek, J. Armston, K. Schindler, R. Dubayah, and J. D. Wegner, "Global canopy height regression and uncertainty estimation from GEDI LiDAR waveforms with deep ensembles," *Remote Sens. Environ.*, vol. 268, Jan. 2022, Art. no. 112760.

[33] M. Drusch et al., "Sentinel-2: ESA's optical high-resolution mission for GMES operational services," *Remote Sens. Environ.*, vol. 120, pp. 25–36, May 2012.

[34] J. Segarra, M. L. Buchaillot, J. L. Araus, and S. C. Kefauver, "Remote sensing for precision agriculture: Sentinel-2 improved features and applications," *Agronomy*, vol. 10, no. 5, p. 641, May 2020.

[35] M. Main-Knorn, B. Pflug, J. Louis, V. Debaecker, U. Müller-Wilm, and F. Gascon, "Sen2cor for Sentinel-2," *Proc. SPIE*, vol. 10427, pp. 37–48, Apr. 2017.

[36] F. Chollet, "Xception: Deep learning with depthwise separable convolutions," in *Proc. IEEE Conf. Comput. Vis. Pattern Recognit. (CVPR)*, Jul. 2017, pp. 1251–1258.

[37] A. Romero, C. Gatta, and G. Camps-Valls, "Unsupervised deep feature extraction for remote sensing image classification," *IEEE Trans. Geosci. Remote Sens.*, vol. 54, no. 3, pp. 1349–1362, Mar. 2016.

[38] B.-S. Hua, M.-K. Tran, and S.-K. Yeung, "Pointwise convolutional neural networks," in *Proc. IEEE/CVF Conf. Comput. Vis. Pattern Recognit.*, Jun. 2018, pp. 984–993.

[39] Z. Zhong et al., "BlockQNN: Efficient block-wise neural network architecture generation," *IEEE Trans. Pattern Anal. Mach. Intell.*, vol. 43, no. 7, pp. 2314–2328, Jul. 2021.

[40] B. X. Jie, M. A. Zulkifley, and N. A. Mohamed, "Remote sensing approach to oil palm plantations detection using xception," in *Proc. 11th IEEE Control Syst. Graduate Res. Colloq. (ICSGRC)*, Aug. 2020, pp. 38–42.

[41] K. Shaheed et al., "DS-CNN: A pre-trained xception model based on depth-wise separable convolutional neural network for finger vein recognition," *Expert Syst. Appl.*, vol. 191, Apr. 2022, Art. no. 116288.

[42] N. Jinsakul, C.-F. Tsai, C.-E. Tsai, and P. Wu, "Enhancement of deep learning in image classification performance using xception with the swish activation function for colorectal polyp preliminary screening," *Mathematics*, vol. 7, no. 12, p. 1170, Dec. 2019.

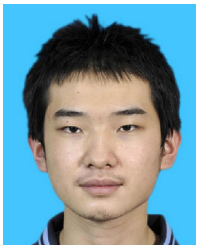
[43] K. He, X. Zhang, S. Ren, and J. Sun, "Deep residual learning for image recognition," in *Proc. IEEE Conf. Comput. Vis. Pattern Recognit. (CVPR)*, Jun. 2016, pp. 770–778.

[44] F. Jiang, F. Zhao, K. Ma, D. Li, and H. Sun, "Mapping the forest canopy height in northern China by synergizing ICESat-2 with Sentinel-2 using a stacking algorithm," *Remote Sens.*, vol. 13, no. 8, p. 1535, Apr. 2021.
[45] I. Fayad et al., "A CNN-based approach for the estimation of canopy heights and wood volume from GEDI waveforms," *Remote Sens. Environ.*, vol. 265, Nov. 2021, Art. no. 112652.
[46] R. Li, S. Zheng, C. Duan, L. Wang, and C. Zhang, "Land cover classification from remote sensing images based on multi-scale fully convolutional network," *Geo-Spatial Inf. Sci.*, vol. 25, no. 2, pp. 278–294, Apr. 2022.
[47] S. Chan, W. Zhou, Y. Lei, C. Li, J. Hu, and F. Hong, "Sparse point annotations for remote sensing image segmentation," *Sci. Rep.*, vol. 15, no. 1, p. 27347, Jul. 2025.
[48] X. X. Zhu et al., "Deep learning in remote sensing: A comprehensive review and list of resources," *IEEE Geosci. Remote Sens. Mag., Replaces Newslett.*, vol. 5, no. 4, pp. 8–36, Dec. 2017.
[49] D. P. Kingma and J. Ba, "Adam: A method for stochastic optimization," 2014, *arXiv:1412.6980*.
[50] T. Swinfield et al., "Imaging spectroscopy reveals the effects of topography and logging on the leaf chemistry of tropical forest canopy trees," *Global Change Biol.*, vol. 26, no. 2, pp. 989–1002, Feb. 2020.
[51] D. R. Roberts et al., "Cross-validation strategies for data with temporal, spatial, hierarchical, or phylogenetic structure," *Ecography*, vol. 40, no. 8, pp. 913–929, Aug. 2017.
[52] W. Luo, Y. Li, R. Urtasun, and R. Zemel, "Understanding the effective receptive field in deep convolutional neural networks," in *Proc. Adv. Neural Inf. Process. Syst.*, vol. 29, 2016, pp. 4898–4906.
[53] S. Kapoor and A. Narayanan, "Leakage and the reproducibility crisis in machine-learning-based science," *Patterns*, vol. 4, no. 9, Sep. 2023, Art. no. 100804.
[54] D. P. Roy, H. B. Kashongwe, and J. Armston, "The impact of geolocation uncertainty on GEDI tropical forest canopy height estimation and change monitoring," *Sci. Remote Sens.*, vol. 4, Dec. 2021, Art. no. 100024.
[55] V. Moudrý et al., "How to find accurate terrain and canopy height GEDI footprints in temperate forests and grasslands?" *Earth Space Sci.*, vol. 11, no. 10, p. 2024, Oct. 2024.
[56] G. F. Watch. (2024). *Global Forest Watch*. Accessed: Mar. 2024. [Online]. Available: https://www.globalforestwatch.org
[57] G. P. Asner and J. Mascaro, "Mapping tropical forest carbon: Calibrating plot estimates to a simple LiDAR metric," *Remote Sens. Environ.*, vol. 140, pp. 614–624, Jan. 2014.
[58] C. Lelli et al., "Biodiversity response to forest structure and management: Comparing species richness, conservation relevant species and functional diversity as metrics in forest conservation," *Forest Ecol. Manage.*, vol. 432, pp. 707–717, Jan. 2019.



Guangpeng Fan received the Ph.D. degree in engineering from Beijing Forestry University, Beijing, China, in 2021.

He has been a Lecturer with Beijing Forestry University since 2021. His research interests include forest LiDAR remote sensing, forest 3-D structure and function parameter extraction, and deep-learning-driven LiDAR combined with multisource data for the extraction of structure parameters of forest vegetation, classification, and mapping.



Binghong Zhang received the B.S. degree in information management and information systems from Beijing Forestry University, Beijing, China, in 2026, where he is currently pursuing the M.S. degree in computer science and technology.

His research interests include computer programming and algorithms, machine learning, and deep learning.



Fei Yan received the Ph.D. degree in forestry equipment and information from Beijing Forestry University, Beijing, China, in 2014.

He is currently an Associate Professor and a M.S. Supervisor with the School of Forestry, Beijing Forestry University. He has led several national and provincial research projects and participated in the field measurement and carbon stock estimation of the tallest known tree in Asia. His research interests include smart forestry, forest carbon sink monitoring, and the integrated applications of 3S technologies (GNSS, remote sensing, and geographic information systems).



Haoran Zhao received the bachelor's degree in computer science and technology from Beijing Union University, Beijing, China, in 2022. He is currently pursuing the master's degree with Beijing Forestry University, Beijing.

His research interests include forest remote sensing, canopy-height estimation, multisource remote sensing data fusion, UAV LiDAR, and artificial intelligence-based analysis of forest structure.



Liangliang Xu received the bachelor's degree in software engineering from Henan University, Kaifeng, China, in 2024. He is currently pursuing the master's degree with Beijing Forestry University, Beijing, China.

His research interests include LiDAR point cloud 3-D reconstruction and remote sensing data-driven deep learning models for tree species classification and invasive species detection.



Jiani Guo received the bachelor's degree in software engineering from Shanxi Agricultural University, Jinzhong, China, in 2024. She is currently pursuing the master's degree with Beijing Forestry University, Beijing, China.

Her research interests include forest LiDAR remote sensing and point cloud modeling of trees.



Jialing Zhou received the B.S. degree in information management and information systems from Beijing Forestry University, Beijing, China, in 2026. She is currently pursuing the M.S. degree in computer science and technology with Northeastern University, Shenyang, China.

Her research interests include artificial intelligence, future Internet technologies, information security, and forestry remote sensing.



Xiangyu Ma is currently pursuing the bachelor's degree in information management and information systems with Beijing Forestry University, Beijing, China.

She integrates information technology to model forest ecological variables and analyze multi-source environmental datasets. Her research interests include remote sensing as well as processing and analysis of ecological data.



Jinhu Wang received the M.S. degree in signal and information processing from the University of Chinese Academy of Sciences, Beijing, China, in 2012, and the Ph.D. degree in optical and laser remote sensing from Delft University of Technology, Delft, The Netherlands, in 2017.

He is currently a Researcher with the University of Amsterdam, Amsterdam, The Netherlands. His research interests focus on object detection and recognition from point cloud data obtained by laser scanning.



Zhiwei Zhang is currently pursuing the Ph.D. degree with Hohai University, Nanjing, China.

He is also with the Key Laboratory of Forest Ecology in Tibet Plateau, College of Resources and Environmental Sciences, Tibet Agricultural and Animal Husbandry University, Nyingchi, China. He has participated in several national and provincial research projects and has published multiple articles in peer-reviewed journals. He also contributed to the book Introduction to Xinjiang Deserts. His research focuses on soil and water conservation and environmental changes in alpine regions, with particular interests in alpine soil erosion processes, desertification mechanisms, ecological restoration, and the application of remote sensing and geographic information systems to environmental monitoring and assessment.



Yan Zhang received the bachelor's degree from Inner Mongolia University, Hohhot, China, in 2003.

She is currently a Professor-Level Senior Engineer with the Xing'an League Institute of Forestry, Ulanhot, China. Her research interests include forest management and forestry remote sensing.



MeiRong Bao received the Ph.D. degree in silviculture from the Central South University of Forestry and Technology, Changsha, China, in 2010.

She is currently with Xing'an Polytechnic University, Horqin Right Front Banner, Inner Mongolia, China. Her research interests include forest resource inventory and monitoring.



Riqian Zhao received the Bachelor of Management degree from Changchun University of Science and Technology, Changchun, China, in 2007.

He is currently with Xing'an Polytechnic University, Horqin Right Front Banner, Inner Mongolia, China. His research interests include agricultural and forestry economic management and smart forestry.



Jia Wang received the B.S. degree in resource environment and urban–rural planning and management and the M.S. degree in physical geography from Harbin Normal University, Harbin, China, in 2003 and 2006, respectively, and the Ph.D. degree in forest equipment engineering from Beijing Forestry University, Beijing, China, in 2009.

He is currently a Professor and Ph.D. Supervisor with the School of Forestry, Beijing Forestry University, where he serves as the Head of the Geographic Information Systems Discipline, the Director of the National First-Class Undergraduate Program in Geographic Information Science, and the Director of Beijing Key Laboratory of Precision Forestry. His research interests include 3S technology integration and applications, precision forestry, forest and grassland carbon sink measurement and monitoring technologies, remote-sensing-based forest structure extraction, ecological and environmental impacts, and vegetation responses to climate change and human activities.



Liangliang Nan received the Ph.D. degree in mechatronics engineering from the Graduate University of the Chinese Academy of Sciences (CAS), Beijing, China, in 2009.

Then, he was an Assistant and later an Associate Professor with Shenzhen Institute of Advanced Technology, CAS, Shenzhen, China. From 2013, he worked as a Research Scientist with the Visual Computing Center, King Abdullah University of Science and Technology (KAUST), Thuwal, Saudi Arabia. In 2018, he joined Delft University of Technology, Delft, The Netherlands, where he is currently an associate professor and co-director of the AI laboratory on 3-D urban understanding (3DUU). His research interests lie at the intersection of computer vision, computer graphics, and 3-D geoinformation, with a focus on understanding and modeling real-world scenes.